Batteries & Supercaps

Research Article
doi.org/10.1002/batt.202400645

Chemistry Europe
European Chemical Societies Publishing

www.batteries-supercaps.org

Assessing Manufacturing-Performance Correlation On $LiMn_{0.7}Fe_{0.3}PO_4$ Electrodes For Application In Upscaled Li-Ion Battery Cells

Luca Minnetti,[a, b, c] Faduma M. Maddar,[c] Anupriya K. Haridas,[c] Matthew Capener,[c] Francesco Nobili,[a, b] and Ivana Hasa*[c]

Olivine $LiMn_xFe_{1-x}PO_4$ (LMFP) cathodes are gaining attention as a promising alternative to $LiFePO_4$ (LFP) for lithium-ion batteries (LIBs), offering higher energy density while maintaining lower costs and improved safety compared to traditional layered oxide cathodes. However, their low electronic conductivity remains a challenge. One effective strategy to enhance electrode kinetics is incorporating carbon additives during fabrication. This study examines the role of conductive additive optimization in $LiMn_{0.7}Fe_{0.3}PO_4$ (LMFP73) electrodes and evaluates the impact of refining the electrode manufacturing to improve performance under practical conditions. Electrodes with 0.5 % single-walled carbon nanotubes (SWCNTs) dispersion demonstrated improved performance. Optimization of mixing protocol, solid content, and coating speed, significantly enhanced the electrode's microstructure, mechanical integrity, and electrochemical response, producing thick electrodes suitable for industrial use. Upscaling to Graphite | LMFP73 single-layer pouch (SLP) cells with 200 g m^{-2} cathode loading resulted in 110 mAh g^{-1} at C/2, retaining 93 % of the initial capacity after 100 cycles. This work provides practical process parameters to reduce the gap between academic and industrial perspectives in electrode performance assessment under realistic conditions, tackling challenges in performance improvement while taking into account high areal loadings, mechanical properties of the coatings, practical electrode balancing, and electrolyte amount in the cell fabrication process.

1. Introduction

Li-ion batteries (LIBs) have been extensively used for energy storage, due to their application versatility from portable electronics to hybrid/full-electric vehicles (HEVs/EVs) and renewable power production plants.[1–3] The popular spread of these systems is attributed to their high energy density, (> 200 Wh Kg^{-1}) remarkable stability and cycle life, which are ascribed to the efficient Li^+ (de−)intercalation mechanism in the electrodes.[4] Nevertheless, the economic and environmental issues associated with the critical transition metals employed in layered oxide cathodes, such as cobalt, has recently shifted trajectory towards the use of alternative cathode chemistries such as the polyanionic phospho-olivine cathodes characterized by outstanding thermal and electrochemical stability, non-toxicity, and lower manufacturing costs.[5,6] Lithium iron phosphate ($LiFePO_4$, LFP), with a specific capacity of 170 mAh g^{-1}, exhibits a relatively lower energy density when compared to commercially available $LiNi_{0.33}Co_{0.33}Mn_{0.33}O_2$ (NMC111).[7] However, its commercialization for automotive and stationary storage has recently soared due to its relevant economic advantage (40 % lower cost) and improved cycling stability compared to the NMC cathodes.[8–11]

To further increase the energy density of olivines, a promising strategy consists of the substitution of Fe with Mn obtaining "mixed-olivine" systems with general formula $LiMn_xFe_{1-x}PO_4$ (LMFP)and theoretical capacity of 170 mAh g^{-1}.[12,13] This multi-metal concept results in a higher energy density than LFP whilst still holding efficient Li^+ transport and hindered pseudo-Jahn-Teller distortion dependent on Mn^{3+}.[14–16] However, the low ionic and electronic conductivity of LMFP is a major hindrance to achieve good rate performance and long cycle life. Various strategies including transition metal doping, tuning of particle size and morphology have been extensively investigated to accelerate the electron transport and ion diffusion in LMFP cathodes.[17–20] Beside bulk material modifications, the low electronic conductivity of olivines has been reported to be mitigated by carbon-coating at the active material level[10,21,22] and/or by the addition of different conductive additives at the electrode formulation level – such as carbon nanotubes (CNTs) or nanowires (CNWs), graphene and conductive binders – in addition to the commonly used nanometric carbon (*i.e.* C65, Super P, carbon black).[23–26]

[a] L. Minnetti, F. Nobili
School of Sciences and Technologies – Chemistry Division, University of Camerino, Via Madonna delle Carceri ChIP, 62032, Camerino, Italy

[b] L. Minnetti, F. Nobili
National Reference Center for Electrochemical Energy Storage (GISEL) – INSTM, Via G. Giusti 9, 50121, Firenze, Italy

[c] L. Minnetti, F. M. Maddar, A. K. Haridas, M. Capener, I. Hasa
WMG, The University of Warwick, Coventry CV4 7AL, United Kingdom
E-mail: ivana.hasa@warwick.ac.uk

Supporting information for this article is available on the WWW under https://doi.org/10.1002/batt.202400645

The combinatorial use of various carbon additives enables different conduction pathways such that carbon black nanoparticles render short-range conduction, while CNTs (or CNWs) provide long-range conduction pathways.[27] Single-walled carbon nanotubes (SWCNTs) are considered ideal conducting agents, owing to their high electrical conductivity (10^6 S m^{-1}), length-diameter aspect ratio (>3500), and excellent mechanical properties (Young's moduli between 270–950 GPa), that could enhance cycling and dimensional stability of electrodes. Nevertheless, large specific surface area of SWCNTs may limit their uniform dispersion in a slurry, causing their aggregation into bundles.[28]

Improved cell performance at high current rates and cycling stability strongly depend on the ionic and electronic conductivity of the electrodes.[29,30] The former one strongly depends on the active materials properties, however, it can also be improved by ensuring an effective contact between electrode particles and the electrolyte enabling fast ion transport through the electrode's porosity.[29,31] Carbon additives play a role in this, defining with their shape and size the voids and contact between active particles and influencing electrolyte penetration into the electrode.[32] Electronic conductivity of the electrode can also be improved by increasing the electrode density, however, beside a certain threshold, this could also lead to an increased tortuosity impairing ion transport. As such, to meet the desired specification for different applications, and for an optimal electrode microstructure, research surrounding manufacturing-performance relationship is of paramount importance as the final electrode microstructure and design contribute significantly to the cell's performance. In this regard, electrode formulation development, slurry processing, and electrode manufacturing play a critical role, especially at the cathode side.[27,33] Parameters such as slurry formulation composition, viscosity, solid content, coating speed, drying temperature, electrode loading, density, and porosity must be optimized to guarantee satisfactory electrochemical performance and cell stability, especially when upscaling from lab-scale to larger cell formats, such as single or multi-layer pouch (SLP and MLP, respectively) or cylindrical cells.[2,33,34] The investigation of these parameters is essential to produce reasonably thick electrodes bridging the gap between academic and industrial perspectives and tackling challenges in performance improvement while taking into account realistic and practical conditions.[33–35]

Several works have reported improved electrochemical response by implementing optimization of the active material's properties, however often not considering the stringent requirements set by industrial applications.[7,13,16,36,37] The comparative assessment of cell performance when transferring the knowledge gained in labs to relevant scales has proven to be challenging especially considering the increased amount of publication in the field adopting testing conditions not applicable to industrial requirements.[34,38]

In this work, we investigate manufacturing-performance correlation aspects of electrode design, reporting on a comprehensive analysis of electrode manufacturing parameters and their effect of cell performance. We assess the impact of SWCNTs addition in the LMFP73 electrode formulation and the effect of various slurry and electrode processing parameters on the overall cell performance at coin cell level and in SLP cells. Different amounts of SWCNTs dispersions were incorporated in the formulation of LMFP73 coatings (indicated as LMFP73-*X*% SWCNT where $X=0$, 0.5, 1, and 2.5). The obtained electrodes were evaluated electrochemically by galvanostatic cycling and analysed in terms of structural and morphological integrity by cross-sectional scanning electron microscopy (cx-SEM) and bendability tests. We investigated the synergy of the mixing strategy, the slurry viscosity and solid content, the coating speed, and the electrode loading in relation to the mechanical and microstructural properties of the electrodes, to obtain industrially relevant optimal coating parameters for electrodes to be implemented both in lab-scale coin-type full cells with graphite anode and upscaled SLPs. The results report a systematic optimization of the slurry mixing and coating process as crucial steps of electrode manufacturing and indicate the importance of the manufacturing-performance correlation on the overall cell performance and cycling stability, particularly when transitioning from lab scale to industrially relevant cell formats.

2. Results and Discussion

The structure and morphology of the carbon-coated commercial LMFP73 active material was evaluated and reported in Figure S1 (Supporting Information). The carbon-coating allows for enhanced electronic conductivity while mitigating potential interfacial side reactions with the electrolyte.[10,13] Figure S1(a) shows a detailed structural investigation of the sample by X-ray diffraction (XRD). Rietveld refinement of the sample reveals phase purity of the LMFP73 material characterized by an orthorhombic cell unit (*Pnma* space group, table N. 62), aligning well with the reference pattern of the olivine lattice (ICSD #193643).[39] The refinement results reported in Table S1 (Supporting Information) show comparable values of the cell unit parameters *a*, *b*, and *c* between LMFP73 and the reference sample, of about 10.4, 6.1, and 4.7 Å, respectively. Furthermore, the unit cell volume of LMFP73 is of about 298.5 Å^3, slightly lower respect to the ICSD reference due to a minor Mn fraction present in the olivine under study.[39,40] The accuracy and the reliability of the refinement are confirmed by the goodness-of-fit parameter (*GOF*) and weighted-profile *R* factor (R_{wp}%), values of <2 and <4, respectively, as provided in Table S1.[41,42] Figure S1(b, c) depicts the morphological properties of the LMFP73 powder, investigated by scanning electron microscopy (SEM). The related SEM images, obtained at different magnifications, reveal the presence of agglomerates of submicrometric primary particles with a size of about 400 nm. Such submicrometric particles can guarantee short diffusion paths for Li^+ ions transport and limit the side reactions with the electrolyte.[10,13]

Research Article
doi.org/10.1002/batt.202400645
Chemistry Europe
European Chemical Societies Publishing

2.1. Investigation of the Impact of SWCNTs Content in LMFP73 Electrodes

Conductive agents are often employed to mitigate the low electronic conductivity of olivine-based cathodes. The use of CNTs as a conductive agent for cathode presents several advantages compared to other carbon additives. The high length-diameter aspect ratio for CNTs compared to other additives allows for instance a lower weight doping level to achieve long range connectivity and contiguous pathways for electrons.[43] This is beneficial both in reducing the weight of inactive materials in the electrode composition and in lowering costs. In this work, we use different amounts of pre-dispersed SWCNTs in a solution of N-methyl-pyrrolidone (NMP) and poly(vinylidene-fluoride) (PVdF) (denoted as SWCNTs dispersion) as conductive additive. Table 1 reports a summary of the different electrode formulations investigated and the resulting slurry properties including sample ID, composition, solid content and viscosity (see Experimental section for further details).

All the investigated formulations incorporated 95% active material to match standards in commercial cells.[27,35,44] Different amounts of SWCNTs dispersion (see Experimental section for compositional details) were added in replacement of C65 carbon additive. The solid content target during formulation development was 48%, which was achieved for all slurries except for LMFP-2.5%SWCNT. Indeed, the rheology of cathode slurries is highly dependent on the carbon black network. Here, a lower solid content was achieved indicating that high content of SWCNTs dispersion limits higher solid content values due to an increased viscosity, related to the PVdF contained in the SWCNTs dispersion, which may result in a reduction of the shear rate, and thus a reduction in the mixing efficiency.[45,46] The formulations shown in Table 1 were used to prepare different slurries with the mixing strategy schematized in Figure 1(a).

In the first step, LMFP73 active material and C65 carbon additive were added into a pot and mixed for 5 mins at 2000 rpm. The addition of PVdF, SWCNTs dispersion, and initial NMP solvent amount followed. After mixing for 5 mins at 2000 rpm, the remaining NMP was added to achieve the targeted solid content and mixed for 5 mins at 2000 rpm. This mixing strategy was chosen as a starting point to investigate the impact of SWCNTs dispersion addition, and further optimisation of the same will be discussed later. The viscosity of the obtained slurries was investigated with the trends of viscosity *vs* shear rate reported in Figure S2 (Supporting Information). The tabulated viscosity values at a shear rate of 10 s^{-1} are reported in Table 1. All the samples followed a similar flow viscosity trend displaying a shear-thinning behaviour, with an initial flat plateau at low shear rates that correspond to the zero-shear viscosity followed by a decrease in shear viscosity at high shear rates.[47] This behaviour generally allows prevention of sedimentation or slumping with breakdown of agglomerates at low shear rates, with a subsequent thin down allowing good processability of the slurry flow in the coater.[35,47] The obtained viscosity of all the samples averaged to ~6.65 Pa·s ± 0.86 satisfactory for electrode processing.[47] Subsequently, the coatings were prepared with a coating speed of 4 mm s^{-1} and a target loading of about 100 g m^{-2} (GSM). Figure 1(b–e) illustrate photographic images of the coatings after calendering to ~30% porosity (for details of calendering process see the Experimental section). All coatings presented inhomogeneous streaks along the surface, which are most likely the result of a not optimized

Table 1. Mixing parameters and properties of LMFP73 slurries with different amount of SWCNTs dispersion containing NMP > 97%, PVdF 2%, dimethyl pyrrolidinone 0.05–0.39%, SWCNTs TUBALL™ 0.4%. Percentage of mixing materials, solid content of the slurry, and viscosity of the slurry at 10 s^{-1} shear rate are reported (see Figure S2 for corresponding viscosity trend).

Sample ID	Mixing material	Percentage	Solid content (SC)	Viscosity (Pa s)
LMFP-0%SWCNT	LMFP73	95%	48%	6.6
	8% PVdF solution	2.5%		
	C65 Imerys	2.5%		
	SWCNTs dispersion	–		
LMFP-0.5%SWCNT	LMFP73	95%	48%	6.7
	8% PVdF solution	2.5%		
	C65 Imerys	2%		
	SWCNTs dispersion	0.5%		
LMFP-1%SWCNT	LMFP73	95%	48%	7.7
	8% PVdF solution	2.5%		
	C65 Imerys	1.5%		
	SWCNTs dispersion	1%		
LMFP-2.5%SWCNT	LMFP73	95%	43.5%	5.6
	8% PVdF solution	2.5%		
	C65 Imerys	–		
	SWCNTs dispersion	2.5%		

Research Article
doi.org/10.1002/batt.202400645
Chemistry Europe
European Chemical Societies Publishing

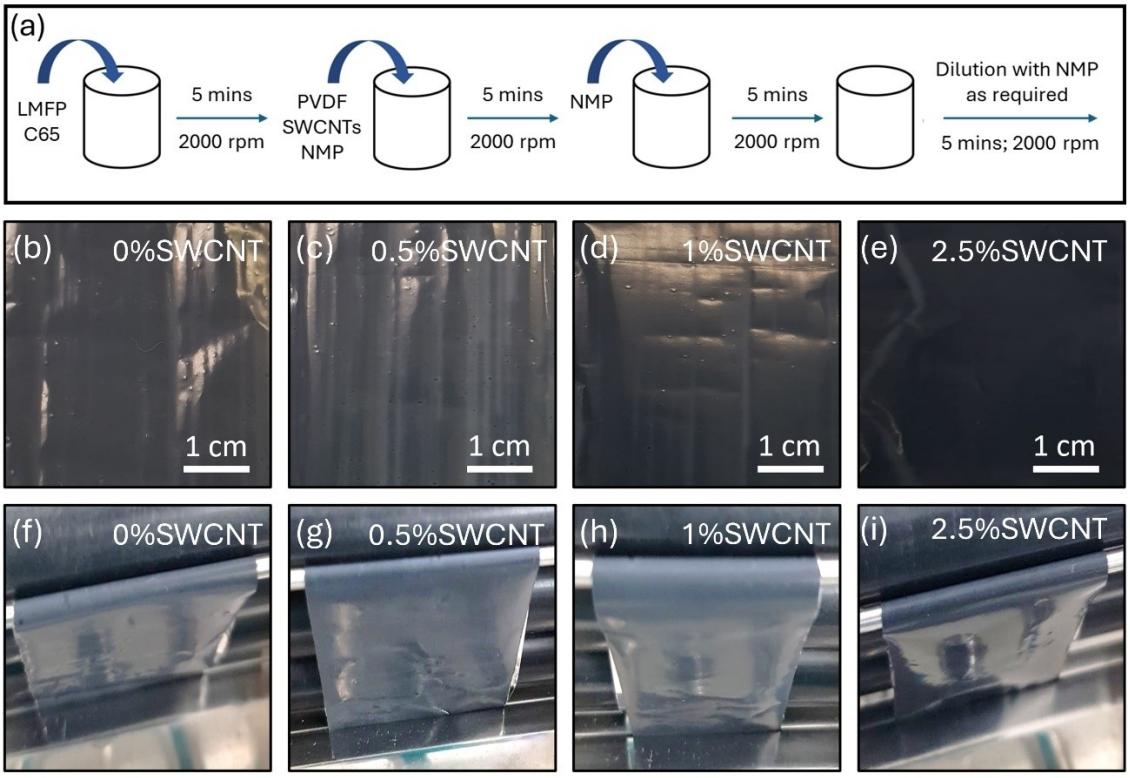

Figure 1. (**a**) Schematic representation of the mixing strategy (see parameters reported in Table 1). Photographic images of the obtained (**b**–**e**) calendered coatings and (**f**–**i**) coating sheets subjected to cylindrical mandrel bend test. In detail: (**b**, **f**) LMFP-0 %SWCNT, (**c**, **g**) LMFP-0.5 %SWCNT, (**d**, **h**) LMFP-1 %SWCNT, and (**e**, **i**) LMFP-2.5 %SWCNT.

particle dispersion and possible formation of C65 and/or SWCNTs aggregates, associated to a difficult initial homogenization of the carbon additives with the adopted mixing strategy. Furthermore, a poor dispersion of nanometric carbon could also influence the dispersion of LMFP73, affecting also dispersion of bigger particles and leading to inhomogeneity across the electrodes.[48] It is worth noting that the content of SWCNTs dispersion used, does not significantly change the quality of the electrodes, except for the LMFP73-2.5 %SWCNT sample which appears to have an improved quality, associated to the lower solid content in the slurry. This ultimately indicates the flaws of the employed mixing strategy and its possible effect on the overall electrode performance, suggesting the necessity to design an improved mixing strategy that can be effectively scaled up. Accordingly, the optimization of several parameters, such as coating speed, mixing time, change of steps of the procedure are required to improve electrodes quality and favour an improved carbon dispersion.[31] It is also important to consider that the rheology of the slurry strongly affects the coating behaviour and the shear rate of the slurry during coating, thus the viscosity of the slurries needs to be optimized considering the coating shear rate.[46,48] The mechanical properties of the coatings were evaluated by using a cylindrical mandrel bend tester, and the photographic images are shown in Figure 1(f–i). Table S2 (Supporting Information) describes the different levels of the bend test, going from no electrode damaging (level 1) to high presence of cracking (level 4).[49] When using a mandrel size of 2 mm diameter, all coatings were shown to have strong adhesion to the aluminium current collector with no signs of delamination or cracking (classified as level 1).

The electronic conductivity of the coatings was also measured with a HIOKI RM2610 device, and the results are reported in Table 2.

The volumetric resistivity for a coating (ρ_V) and the interface resistance between a coating and the current collector (R_{int}) can be calculated by the instrument via a finite volume model. The total through-plane resistance (R_T) was calculated from the values tabulated in Table 2 using Equation (1):

$$R_T = (\rho_V * s_C) + R_{int} \quad (1)$$

where s_C is the coating thickness. Subsequently, the through-plane conductivity (σ_T) can be calculated from the obtained R_T values. The results show low overall values of R_T for all the samples, attributed to an effective calendering process, which improves the contact between the particles in the electrodes and the current collector and leads to a denser particle arrangement and improved contact between the conductive additive and the active material, resulting in a subsequent decrease in the interface resistance,[50,51] as already reported for olivine cathodes.[27,51,52] Nevertheless, the through-plane conductivity (σ_T) increases as the SWCNTs dispersion content increases up to 1 %, to then slightly decrease for the LMFP73-

Research Article
doi.org/10.1002/batt.202400645
Chemistry Europe
European Chemical Societies Publishing

Table 2. Results of electrode resistance, resistivity, and conductivity measurements of LMFP73 coatings with different amount of SWCNTs in terms of electrode composite layer volume resistivity (ρ_V), interface resistance between the composite layer and the current collector (R_{int}), with related standard deviation (SD), calculated total through-plane resistance (R_T) (see Equation (1)), and calculated through-plane conductivity (σ_T), with corresponding coating thickness.

Sample ID	ρ_V (Ω cm)	SD	R_{int} (Ω cm^2)	SD	R_T (Ω cm^2)	Coating thickness (μm)	σ_T (S cm^{-1})
LMFP-0%SWCNT	25.2 ± 1.6	1.8	5.2 ± 1.4	2.3	5.32 ± 0.91	44	8.27×10^{-4}
LMFP-0.5%SWCNT	5.9 ± 0.2	0.3	2.8 ± 0.5	0.8	2.82 ± 0.43	44	1.56×10^{-3}
LMFP-1%SWCNT	3.9 ± 0.5	0.6	1.1 ± 0.2	0.4	1.12 ± 0.21	43	3.84×10^{-3}
LMFP-2.5%SWCNT	5.5 ± 0.2	0.2	2.5 ± 0.1	0.2	2.52 ± 0.13	43	1.71×10^{-3}

2.5%SWCNT sample which presents no C65 additive. It is worth noting that the conductivity of the coating containing 2.5% SWCNT dispersion is higher than the coating with only C65 (*i.e.* LMFP73-0%SWCNT) which indicates the enhanced effectiveness of SWCNTs as compared to C65 when it comes to electronic conductivity.[52] Nevertheless, the overall increased resistance observed in the presence of high amounts of SWCNTs dispersion (2.5%) can arise from the mixing strategy used resulting in particle agglomeration linked to the strong inter-tube attraction among CNTs, leading to localized electrical disconnections within the electrode.[28,53–55] This clearly highlights the advantage of having both SWCNTs and C65 in the electrode formulation, which allows the building of a three-dimensional conduction framework in the electrode. The structural integrity and homogeneous distribution of the electrode components of the prepared coatings were investigated by examining electrode cross-sections using SEM coupled with energy dispersive X-ray spectroscopy (EDS) as illustrated in Figure 2.

The cross-sectional images of the electrodes containing 0% SWCNTs dispersion reveal the presence of particle agglomerates resulting in large particles clusters across various parts of the electrode, as indicated by the red arrows in Figure 2(a, b). With the addition of SWCNTs to the formulation, a more homogenously distributed mixture was obtained indicating the synergetic effects of using both C65 and CNTs. Carbon agglomerates are also highlighted in the EDS images (Figure 2(e)) of the lower magnification SEM images (Figure 2(c)). EDS carbon maps with higher magnifications, reported in Figure S3(b, c) (Supporting Information) illustrate a more continuous conductive network between the active material particles across the electrode as compared to the electrodes containing 0% SWCNTs (Figure S3(a)), where regions of no carbon network are encountered as highlighted by the white arrows. Indeed, electrodes containing 0.5 and 1% of SWCNTs dispersion, show carbon agglomerates (brighter regions) associated with the strong clustering tendency of CNTs (see C maps in Figure 2 and Figure S3). However, for the electrodes with 2.5% SWCNTs dispersion (Figure 2(s–t)), the presence of electrode cracking (indicated by the yellow arrows) and a partial detachment from the current collector (see Figure 2(s)) was observed. The complete removal of C65 and the exclusive use of SWCNTs in the formulation results in a reduction of point-to-point contact, which is typically observed between carbon black (*i.e.* C65) and active

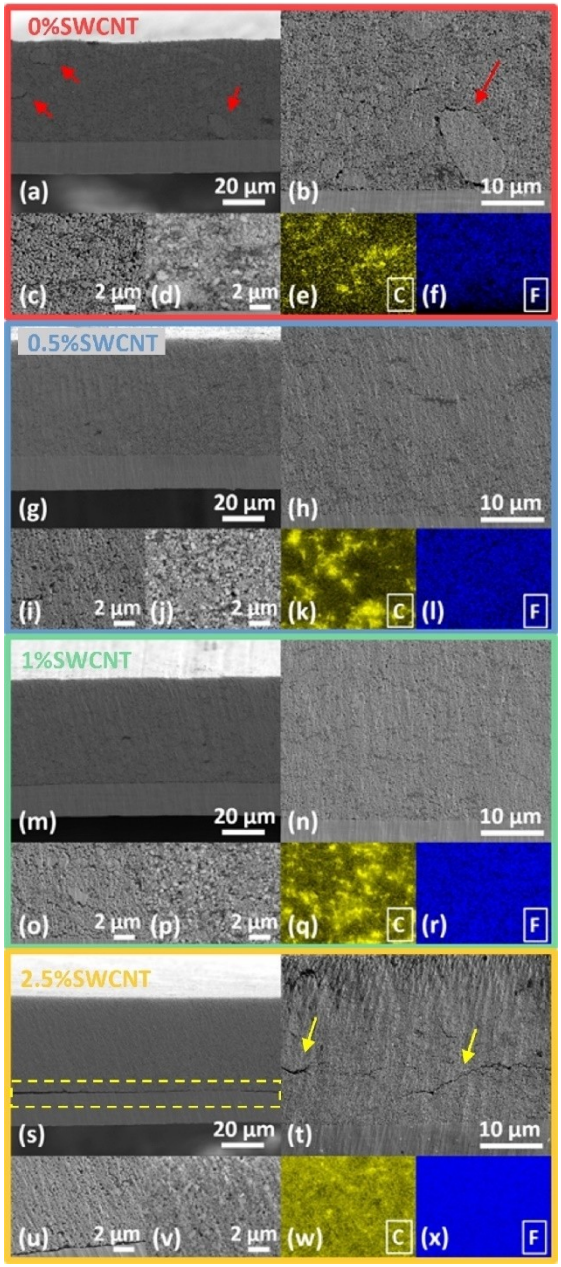

Figure 2. Cross-sectional scanning electron microscopy (cx-SEM) and correlated energy dispersive X-ray spectroscopy (EDS) analyses of LMFP73 coatings with different amount of SWCNTs. In detail: cx-SEM images at different magnifications of (**a**–**d**) LMFP-0%SWCNT, (**g**–**j**) LMFP-0.5%SWCNT, (**m**–**p**) LMFP-1%SWCNT, and (**s**–**v**) LMFP-2.5%SWCNT with related SEM-EDS elemental maps of (**e**, **k**, **q**, **w**) C and (**f**, **l**, **r**, **x**) F, respectively.

Research Article
doi.org/10.1002/batt.202400645
Chemistry Europe
European Chemical Societies Publishing

material particles, and an increase in line-to-line contact between CNTs leading to an overall poorer contact between the electrode particles and/or to current collector.[54,56] In addition, the EDS carbon map shown in Figure 2(w) and Figure S3(d) illustrates the accumulation of carbon on the electrode surface proving poor conductive network throughout the electrode. This carbon accumulation could be related to sedimentation of heavier particles, probably ascribed to the additional amount of PVdF binder included in the slurries by adding increasing amounts of SWCNTs dispersion, which also contains PVdF. This is also evidenced by the EDS fluorine map reported highlighting an increase of fluorine content from electrodes containing 0% SWCNTs to 2.5% SWCNTs. (see Figure 2 panels f, l, r, x, respectively).[45] This behaviour further limits the ion/electronic transport and rate performance especially in high loading electrodes.[35]

Overall, the preliminary evaluation of the prepared electrode coatings suggests the need to further optimize the slurry and electrode processing parameters to improve the distribution between the active material, conductive additive and binder system in the electrode. However, to better understand the manufacturing-performance relationship, electrochemical testing of the prepared coatings was conducted to evaluate the effect of varying SWCNTs dispersion content and their deriving electrode properties on their electrochemical response. Figure 3 reports the electrochemical response of the prepared LMFP electrodes.

As a representative standard system, electrodes containing 0% SWCNTs dispersion were first used to benchmark the electrochemical processes using cyclic voltammetry (CV) and galvanostatic intermittent titration technique (GITT). Figure 3(a) shows the voltammogram of the LMFP73-0%SWCNT electrode exhibiting the characteristic anodic peaks centred at 3.6 and 4.15 V *vs.* Li^+/Li indicating the oxidation (de-lithiation) process, and the cathodic peaks centred at 3.45 and 3.9 V *vs.* Li^+/Li indicating the reduction (lithiation) process. The peaks at 3.6 and 3.45 V *vs.* Li^+/Li are ascribed to the Fe^{2+}/Fe^{3+} redox couple, while those at 4.15 and 3.9 V *vs.* Li^+/Li are attributed to the Mn^{2+}/Mn^{3+} redox activity in LMFP73. It can be noted that the Fe and Mn redox couples are observed at slightly higher and lower potentials, respectively, compared to the bare $LiFePO_4$ and $LiMnPO_4$, aligning well with previous reports on mixed olivine cathodes.[13,57] The observed shift of the transition metal redox potentials can be attributed to changes in the ionic character and distance of the M–O bond promoted by transition metal substitution.[57] Furthermore, the CV curves reveal considerable reversibility, modest polarization, and fairly fast Li^+ (de−)insertion kinetics process for the LMFP73 material.[58] To further investigate the ion transport kinetics, Li^+ diffusion coefficient was determined, according to the method proposed by Weppner and Huggins.[59] Prior to the experiment, four galvanostatic cycles have been performed to allow interphase stabilization and minimize material activation effects. Figure S4 (Supporting Information) depicts the time evolution of the potential during titration (black curve), obtained by applying repeated current pulses/potential relaxation steps. A constant current of C/10 (1 C = 170 mA g^{-1}) is used to assume the diffusion process in the surface layer, as evidenced in the

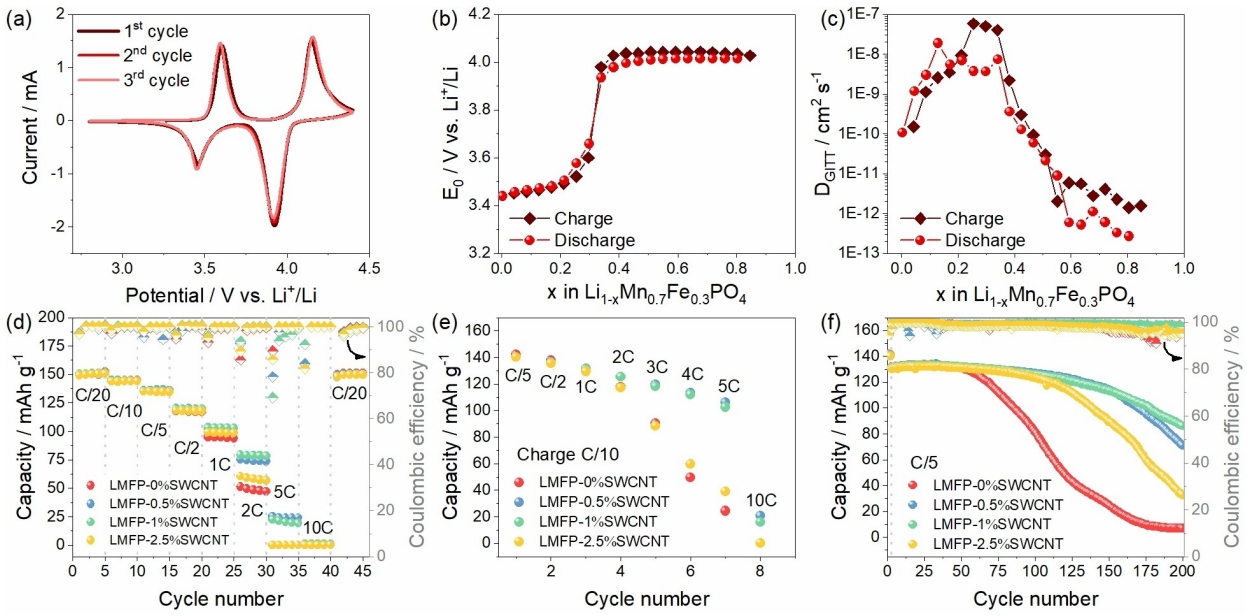

Figure 3. Electrochemical characterization of LMFP73 coatings with different amount of SWCNTs in Li half-cell at 25 °C. (**a**) CV profiles of LMFP-0%SWCNT. Potential range 2.8–4.4 V *vs.* Li^+/Li; scan rate 0.05 mV s^{-1}. (**b**) Trend of E_0 *vs. x* for LMFP-0%SWCNT determined from GITT curve (see Figure S2 Supporting information). (**c**) Trend of D_{GITT} *vs. x* for Li^+ ions calculated using Equation (S2) (Supporting Information). Applied pulses current: 17 mA g^{-1} (0.1 C rate); potential range 2.8–4.4 V *vs.* Li^+/Li. Cycling trend of (**d**) rate capability test performed at C/20, C/10, C/5, C/2, 1 C, 2 C, 5 C, and 10 C currents (1 C = 170 mA g^{-1}) with discharge capacity in left-hand side *y*-axes and coulombic efficiency in right-hand side *y*-axes, (**e**) alternate current rate capability test performed charging the cell at C/10 and discharging it at C/5, C/2, 1 C, 2 C, 3 C, 4 C, 5 C, and 10 C currents, and (**f**) prolonged galvanostatic test performed at the constant current rate of C/5 after 2 activation cycles at C/10 with discharge capacity in left-hand side *y*-axes and coulombic efficiency in right-hand side *y*-axes. Voltage range 2.8–4.4 V.

Weppner and Huggins procedure.[59] The figure also shows the overlap of the quasi-equilibrium potential profiles (E_0) during charge (dark red) and discharge (light red) after relaxation. The trend of E_0 *vs.* x (exchange lithium degree in $Li_{1-x}Mn_{0.7}Fe_{0.3}PO_4$) is reported in Figure 3(b) and shows a reversible titration extended up to $x = 0.84$ under quasi-equilibrium conditions, which confirms high electrochemical activity and the beneficial effect of iron incorporation in $LiMn_{1-y}Fe_yPO_4$ phase on the Li^+ reversible exchange ability.[15,60] The lithium diffusion coefficient, D_{GITT} ($cm^2\ s^{-1}$), was calculated using the data reported in Figure 3(b) and applying Equation (S2)[59] reported in the Supporting Information section.

Figure 3(c) reports the D_{GITT} during de-lithiation as a function of x for LMFP73. The results show the typical trend commonly reported for mixed olivine cathodes with a general decrease of diffusion coefficients for the de-lithiated phase at high x.[60,61] In particular, the figure depicts an initial increase of D_{GITT} in charge to a maximum value of $\sim 5\times10^{-8}\ cm^2\,s^{-1}$ at $x = 0.3$, followed by a sharp decrease as x increases to a minimum value of $\sim 10^{-12}\ cm^2\,s^{-1}$. Furthermore, D_{GITT} during discharge (lithiation) are slightly smaller than the values obtained during charge, likely due to the insulating character of the de-lithiated phase. Overall, the obtained D_{GITT} values for LMFP73 are slightly higher but comparable with those achieved in other studies focusing on mixed olivines, suggesting favourable Li^+ diffusion kinetics.[60,61]

The effect of SWCNTs dispersion amount on the electrochemical performance of LMFP73 electrodes was evaluated in Li half-cells, using 1 M $LiPF_6$ in EC:EMC (3 : 7 (v/v%)) with 1 wt% VC containing electrolyte and 100 GSM electrode loading. The corresponding data are reported in Figure 3(d–f). Rate capability tests of the four samples were carried out by increasing the current from C/20 to 10 C ($1\ C = 170\ mA\,g^{-1}$) as shown in Figure 3(d). All samples exhibited an initial capacity of about $150\ mAh\,g^{-1}$ (88% of the theoretical value) that reduced to about $2\ mAh\,g^{-1}$ at 10 C. However, an excellent recovery of the initial capacity was observed in all the samples as the current was reduced back to C/20 after the consecutive cycles, indicating good rate capability and the stability of LMFP73 material upon the stress caused by high current loads.[29] Moreover, at high currents (above 1 C), the electrodes containing 0.5% and 1% SWCNTs dispersion, outperformed the bare electrodes without SWCNTs exhibiting higher capacity retention. Indeed, the 2.5%SWCNT electrodes (no C65 additive) resulted in poor performance at such higher rates as compared to electrodes with both C65 and SWCNTs additives, in agreement with the conductivity data and the SEM cross-sectional analysis reported in Table 2 and Figure 2, respectively. To further investigate the effect of SWCNTs on the performance, an alternative rate capability test was performed in which the cell is charged at C/10 and discharged with increasing current loads up to 10 C. Figure S5 (Supporting Information) reports the voltage profiles corresponding to the electrodes obtained with the four formulations suggesting an increase in polarization as a consequence of current increase which lead to a decrease of discharge capacity from $140\ mAh\,g^{-1}$ at C/5 for all the samples to about $20\ mAh\,g^{-1}$ at 10 C for LMFP73-0.5%SWCNT and LMFP73-1%SWCNT. The 2.5%SWCNT electrodes show a prominent degradation over cycling at increasing rates. The cycling trend shown in Figure 3(e) is a further evidence of the beneficial effect of SWCNTs incorporation, with the 0.5% and 1% SWCNTs dispersions containing electrodes maintaining discharge capacity values higher than $100\ mAh\,g^{-1}$ up to 5 C current. The stability of the electrochemical lithium (de−)insertion process is investigated by galvanostatic cycling at a constant rate of C/5 after 2 activation cycles performed at C/10. The corresponding voltage profiles (see Figure S6, Supporting Information) reveal the expected shape for all the samples characterized by two well-defined plateaus at an average voltage of 3.55 and 4.1 V, ascribed to the Fe^{2+}/Fe^{3+} and Mn^{2+}/Mn^{3+} redox couples, respectively, in agreement with the CV of Figure 3(a), emphasising that CNTs serve mainly as conductive additives without direct participation in the electrochemical process. Furthermore, the profiles show a maximum capacity of about $130\ mAh\,g^{-1}$, in full agreement with the rate capability results. The cycling trend reported in Figure 3(f) manifests different cycling stability for the different coatings. In particular, all samples present the same capacity trend up to about 75 cycles, where then the 0% SWCNT electrodes show a very rapid decrease in capacity up to complete deterioration. This is likely associated to the lower electronic conductivity and the poor mixing dispersion during electrodes processing, as evidenced earlier.[16] It is worth noting that the 2.5%SWCNT electrodes cycle longer, with capacity decays observed after about 125 cycles, indicating further the advantage of using solely CNTs rather than only C65.[62] Furthermore, the cells with intermediate amount of SWCNTs, *i.e.* LMFP73-0.5%SWCNT (blue dots) and the LMFP73-1%SWCNT (green dots), reveal better stability, with the latter one exhibiting an improved retention of about 67% after 200 cycles. Moreover, all the cells report coulombic efficiency of about 96% in the first activation cycle which further increases and reaches about 99% in the subsequent ones.

The results of the formulation effect on LMFP73 cathode indicates LMFP73-0.5%SWCNT and LMFP73-1%SWCNT as the most promising candidates for further applications, with the latter presenting slightly higher conductivity and prolonged cycling stability with respect to the former. Nevertheless, both electrodes reach 80% of the initial capacity retention, considered as a threshold value of state of health,[34] after 170 cycles. Considering the economic benefits of including less inactive materials and the satisfactory electrochemical performance, the 0.5%SWCNT formulation was selected over the LMFP73-1% SWCNT for further optimization studies.[34,44]

2.2. Investigation of the Impact of Slurry and Electrode Processing Parameters

The effect of the slurry mixing and coating parameters were investigated with the LMFP73-0.5%SWCNT electrode formulation optimized in the previous section. To improve the quality of the slurry mixing and resultant electrode coatings, the mixing procedure was modified by altering the sequence of slurry component addition while mixing (denoted as Mixing #2,

Research Article
doi.org/10.1002/batt.202400645
Chemistry Europe
European Chemical Societies Publishing

Figure 4(a)) and compared with the previous mixing strategy (denoted as Mixing #1, see Figure 1(a)) at 50 % solid content.

The modified mixing strategy, *i.e.* Mixing #2, includes an additional initial step involving an initial mixing of C65 in NMP to further improve carbon distribution within the mix and avoid particle agglomeration, thus improving slurry processability.[27] In more detail, C65 and the first part of NMP were added into a pot and mixed for 5 mins at 2000 rpm. LMFP73 and the second part of NMP were then added and mixed for 5 mins at 2000 rpm. This was then followed by the addition of PVdF, SWCNTs dispersion, and the third part of NMP then mixed for 5 mins at 2000 rpm. The final remaining NMP was added in one or several times and mixed for 5 mins at 2000 rpm to achieve the target solid content. The viscosity *vs.* shear rate profiles of the slurries obtained using the two mixing procedures (Figure 4(b)) presented similar trends exhibiting viscosity values of 7.8 Pa·s at 10 s^{-1} for both mixing procedures. The slightly higher viscosity values compared to the one obtained previously for the LMFP73-0.5 %SWCNT formulation (see Table 1) are due to the higher solid content adopted with Mixing #2. Further, the slurry coating speed was investigated to improve the homogeneity of the electrode coatings.[31] The electrode loadings achieved with various coating speeds were plotted and compared as shown in Figure 4(c). It is worth noting that coatings prepared at various speeds via Mixing #1 exhibited slightly higher electrode loadings compared to the analogous coatings prepared with Mixing #2, which can be attributed to the flaws in Mixing #1 that resulted in the non-homogenous dispersion of particles and larger variations in electrode loading (see Figure 4(d–k)). Even though the electrode loadings prepared with both the mixing strategies follow a linearly increasing trend with an increase in coating speed, considering

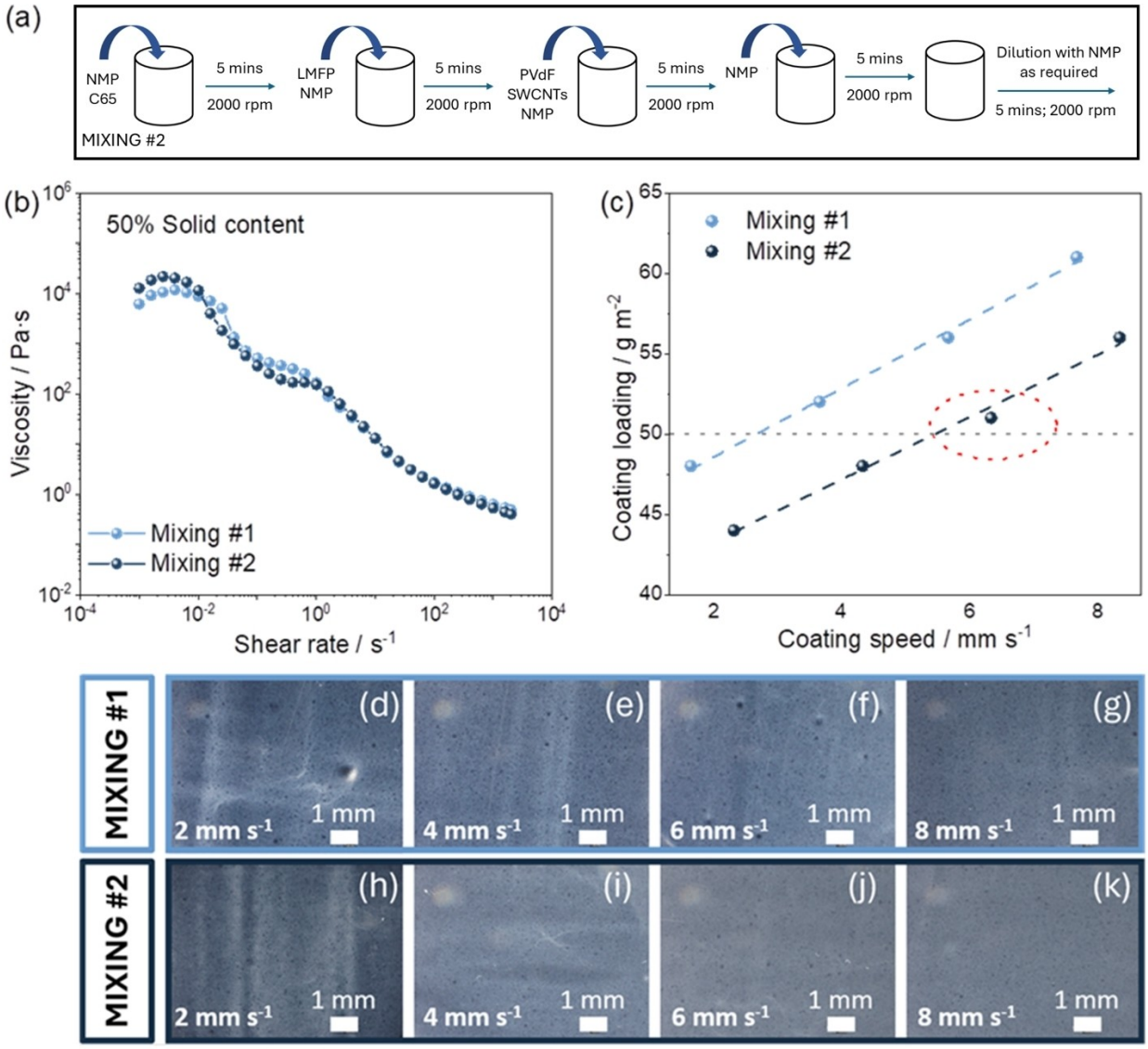

Figure 4. Processing and manufacturing optimization of LMFP-0.5 %SWCNT in terms of mixing and coating parameters. (**a**) Schematic representation of Mixing #2 procedure (see Figure 1(a) for Mixing #1 scheme). (**b**) Trend of viscosity *vs.* shear rate of the slurries obtained from the two mixing strategies. (**c**) Trend of coating loading *vs.* coating speed of the samples obtained from the two mixing strategies. Optical microscope images of coatings obtained using (**d**–**g**) Mixing #1 and (**h**–**k**) Mixing #2 casted at different speeds. In detail: (**d**, **h**) 2 mm s^{-1}, (**e**, **i**) 4 mm s^{-1}, (**f**, **j**) 6 mm s^{-1}, (**g**, **k**) 8 mm s^{-1}.

Research Article
doi.org/10.1002/batt.202400645
Chemistry Europe
European Chemical Societies Publishing

a target loading of 50 GSM, the coatings prepared with Mixing #2 at 6 mm s^{-1} achieved an electrode loading closer to the target and were selected for further process optimizations. Furthermore, the optical microscopy images of the calendered coatings prepared with Mixing #1 and Mixing #2 are shown in Figure 4(d–g) and Figure 4(h–k) respectively. The coatings prepared with Mixing #2 exhibited improved homogeneity associated with an efficient dispersion of the slurry components while particle agglomerates and streaks were observed in the coatings prepared with Mixing #1. The effect was more evident for slower coating speeds. Indeed, the electrodes prepared with the lowest coating speed (*i.e.* 2 mm s^{-1} and 4 mm s^{-1}) for both Mixing #1 (Figure 4(d, e)) and #2 (Figure 4(h, i)) revealed inhomogeneous areas evidenced by brighter lines visible in the images. Instead, the electrodes prepared with coating speeds of 6 and 8 mm s^{-1} via Mixing #2 (Figure 4(j, k)) exhibited improved homogeneity without defects observed on the electrodes' surface. All the coatings analysed displayed good bendability with a mandrel size of 2 mm diameter as demonstrated in Figure S7(a–h) (Supporting Information), indicating the absence of flaking and damage to the electrodes (level 1, see Table S2).

As solid content represents a critical parameter in formulation development studies, affecting rheology, mixing efficiency and homogeneity of the slurries, further studies were conducted to evaluate its effects.[33] To determine the impact of solid content, the mixing strategy and the coating speed of the formulations were fixed as previously optimised (Mixing #2, 6 mm s^{-1}) and three different solid contents, *i.e.* 40 %, 50 %, and 60 %, for the LMFP73-0.5 %SWCNT formulation were investigated.

Figure 5(a) reports the viscosity trends of the three electrode formulations, where a higher viscosity is observed for the formulation with 60 % solid content and comparatively lower viscosities are observed as the solid content goes down to 40 %. The observed viscosity values for 40 %, 50 %, and 60 % solid content are 2.1, 12.9, and 72.2 Pa·s respectively at 10 s^{-1}, highlighting the importance of slurry viscosity to guarantee good processability of the electrode coatings, particularly at higher solid contents.[47] The photographic images of the calendered electrode coatings (Figure 5(b–d)) with a target electrode loading of 50 GSM and their corresponding mandrel bend test (Figure 5(e–g)) exhibit severe surface inhomogeneity at 60 % solid content (Figure 5(d)) compared to 40 % and 50 % (Figure 5(b) and 5(c), respectively), ascribed to the improper mixing and agglomeration of the slurry components at higher solid content. All the electrode samples exhibit good bendability with a 2 mm mandrel, owing to the low target electrode loading (50 GSM), as observed previously. Further, the quality of the electrode coatings with varying solid content was evaluated by assessing the cx-SEM images of the electrodes recorded after calendering. The electrode obtained with 60 % solid content exhibited significantly large darker areas (Figure 5(j)) ascribed to the agglomerates of SWCNTs generated as a result of the inefficient mixture of the slurry components. The electrode coatings with 40 % solid content revealed evident discontinuities consisting of voids and cracks (Figure 5(h), indicated with

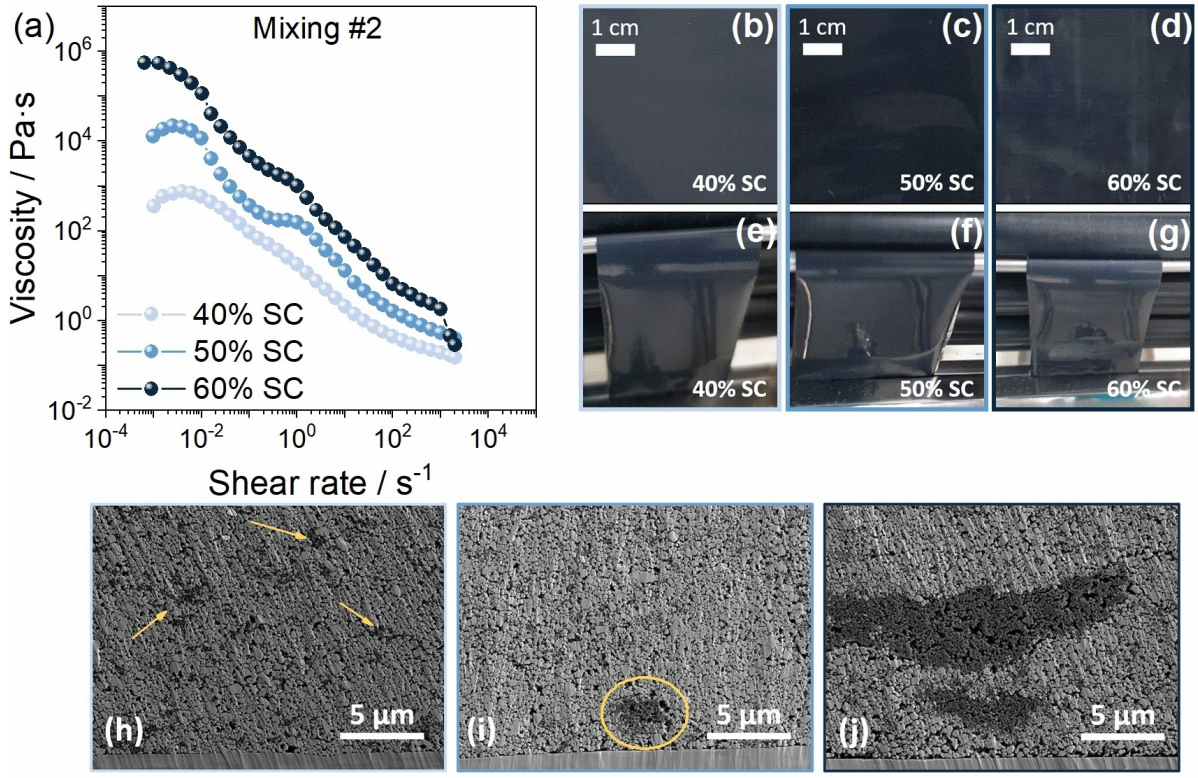

Figure 5. Effect of solid content in formulation optimization of LMFP-0.5 %SWCNT slurries. Mixing #2, coating speed 6 mm s^{-1}. (**a**) Trend of viscosity *vs.* shear rate of the slurries prepared with the three selected solid content. Photographic images of (**b**–**d**) electrode coatings and (**e**–**g**) coatings subjected to cylindrical mandrel bend test. In detail: (**b**, **e**) 40 % SC, (**c**, **f**) 50 % SC, (**d**, **g**) 60 % SC. cx-SEM images of (**h**) 40 % SC, (**i**) 50 % SC, and (**j**) 60 % SC electrodes.

Research Article
doi.org/10.1002/batt.202400645
Chemistry Europe
European Chemical Societies Publishing

yellow arrows) formed due to weak inter-particle cohesion and the lack of optimal adhesion between the particles and the current collector ascribed to the dilute and flowy liquid-like slurry at low solid contents.[27] At 50% solid content, the electrode exhibited the best homogeneity without any crack formation (Figure 5(i)) compared to 40% and 60% solid contents. However, small, less occurring areas of non-homogenously distributed carbon were observed in the electrode (highlighted with a yellow circle), suggesting the requirement for further solid content optimization. The best compromise to viscosity, optimal mixing and particles cohesion was identified when adopting 46% solid content retaining a processable viscosity of 6.8 Pa·s at 10 s^{-1} (see Figure S8 Supporting Information for the viscosity trend).

The electrochemical performance of LMFP73-0.5%SWCNT electrodes (46% solid content) was evaluated, and the comparative results obtained with coatings produced before optimization (see Figure 1 for details) are reported in Figure 6.

The photographic images of the coatings before and after optimization, reported in Figure 6(a) and 6(b) respectively, reveal an evident improved quality of the electrodes. Defect-free coatings were attained with the optimized mixing procedure against the surface inhomogeneity characterizing the coating obtained with the first mixing strategy. However,

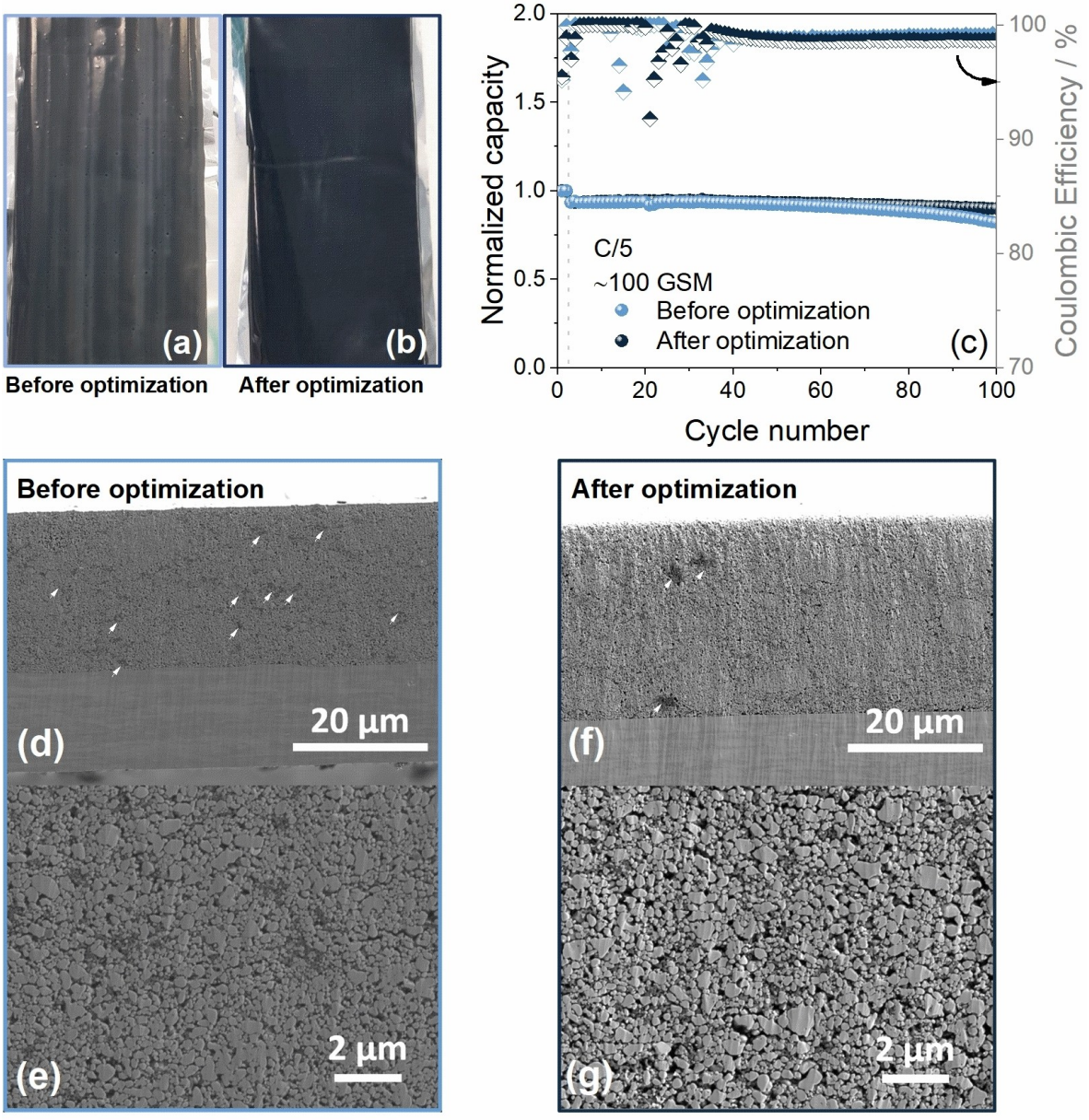

Figure 6. Comparison of LMFP-0.5%SWCNT coatings properties before and after optimization. Photographic images of coating sheets (**a**) before and (**b**) after the optimization process. (**c**) Electrochemical performance in Li-cell at 25 °C in terms cycling trend of prolonged galvanostatic test performed at the constant current rate of C/5 (1 C = 170 mA g^{-1}) after 2 activation cycles at C/10 with normalized discharge capacity in left-hand side *y*-axes and coulombic efficiency in right-hand side *y*-axes. Voltage range 2.8–4.4 V. cx-SEM images of the electrodes at different magnification (**d**, **e**) before and (**f**, **g**) after the optimization process.

Research Article
doi.org/10.1002/batt.202400645
Chemistry Europe
European Chemical Societies Publishing

this difference was not clearly reflected at the microstructural level or in the electrochemical response observed in coin cells. The cycling trend of the cells is reported in Figure 6(c) with normalized capacities to avoid the possible capacity discrepancies due to small variations of electrode loadings (gravimetric capacity at the first cycle is 141 mAh g^{-1} and 145 mAh g^{-1} for the electrodes before and after optimization, respectively, as shown in galvanostatic profiles of Figure S9 Supporting Information). The cells exhibit similar capacity retention until 80 cycles (88% and 95% before and after optimization, respectively), with a coulombic efficiency of 95% in the first activation cycle further increased from about 97% to 99% during the subsequent cycles. It is worth mentioning that the low coulombic efficiencies observed are attributed to an unstable solid-electrolyte interphase (SEI) at the lithium metal electrode and that higher efficiencies are expected in full coin cell as it will be shown later. In addition, between cycles 20–40 destabilized efficiency was observed that may be ascribed to possible gas evolution inside the cells.[63] Moreover, the cx-SEM images of the coatings before (Figure 6(d, e)) and after (Figure 6(f, g)) optimization depict a similar morphology of the electrodes, without the presence of significant cracking or inhomogeneity, with the electrodes obtained before optimization showing several small agglomeration of particles (some of them highlighted by white arrows in Figure 6(d)) and the electrode obtained after optimization showing a reduced number of agglomerates, however with larger areas. While the differences observed at coin cell level may be considered minor, it is important to consider that the electrochemical performance would be significantly impacted if evaluated in large-format cells employing electrodes prepared with the first mixing strategy, highlighting the challenges and complexity involved in scaling up electrode production. Inhomogeneous electrode appearance may indeed strongly affect cell performance especially of cylindrical cells, that require larger and longer area of electrode homogeneity even when compared to pouch cell formats.[2,34,38]

2.3. Investigation of the Impact of Electrode Loading and Upscaling to Single Layer Pouch Cells

The optimised electrodes obtained with LMFP73-0.5%SWCNT formulation prepared via Mixing strategy #2 at a coating speed of 6 mm s^{-1}, and 46% solid content were adopted to produce coatings with higher electrode loadings up to 250 GSM and the corresponding electrochemical response was evaluated at coin cell level and reported in Figure 7.

The electrodes' mechanical properties were evaluated through cylindrical mandrel bend test and the photographic images are reported in Figure 7(a–d). The coatings exhibited lower bendability at higher electrode loadings, as expected. The electrode coating with 100 GSM (Figure 7(a)) displayed good bendability with no flaking or damage (level 1, see Table S2) while the 250 GSM coating (Figure 7(d)), revealed severe cracking and flaking (level 4, see Table S2). The poor mechanical features can affect the structural integrity of electrodes leading to cracking, delamination, and poor electrical contact, which can significantly hinder the electrochemical performances and reduce the cycle life, negating the benefits achieved with increased active material content.[49] The electrochemical response of the prepared LMFP73-0.5%SWCNT high loading electrodes was evaluated in Li half-cells by galvanostatic cycling, with results shown in Figure 7(e, f). Rate capability tests

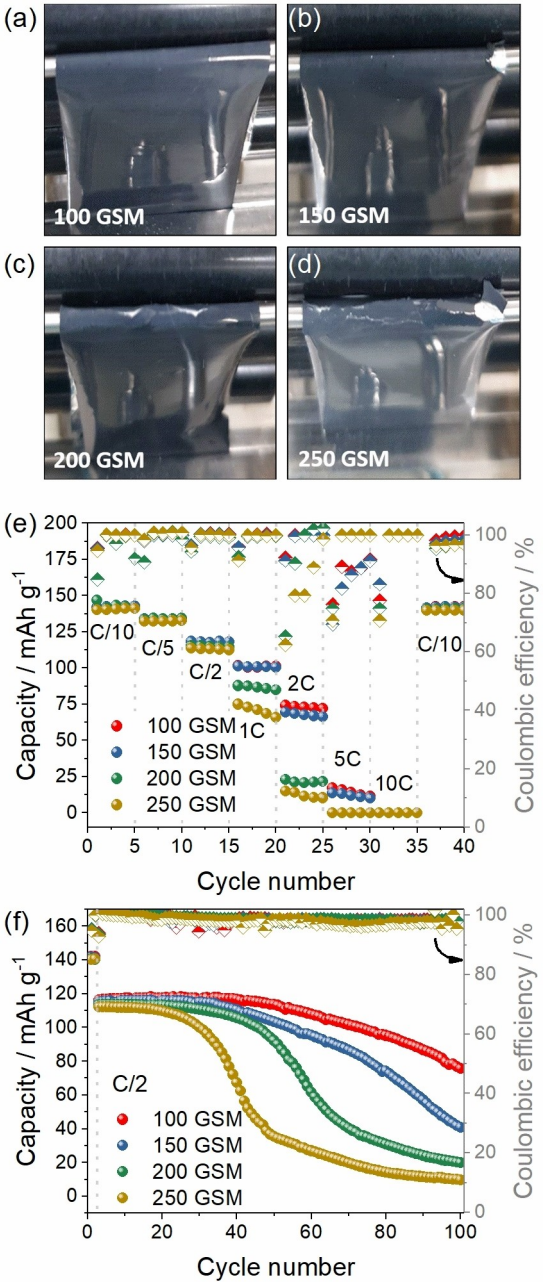

Figure 7. Mechanical and electrochemical characterization in Li half-cell at 25 °C of LMFP-0.5%SWCNT electrodes with different loadings. (**a–d**) Photographic images of coating sheets subjected to cylindrical mandrel bend test. In detail: (**a**) 100 GSM, (**b**) 150 GSM, (**c**) 200 GSM, (**d**) 250 GSM. Cycling trend of (**e**) rate capability test performed at C/10, C/5, C/2, 1 C, 2 C, 5 C, and 10 C currents (1 C = 170 mA g^{-1}) and (**f**) prolonged galvanostatic test performed at the constant current rate of C/2 after 2 activation cycles at C/10 with discharge capacity in left-hand side *y*-axes and coulombic efficiency in right-hand side *y*-axes. Voltage range 2.8–4.4 V.

Research Article
doi.org/10.1002/batt.202400645
Chemistry Europe
European Chemical Societies Publishing

were carried out by progressively increasing the current from C/10 to 10 C (1 C = 170 mA g^{-1}) and finally switching back to C/10 as reported in Figure 7(e). The corresponding voltage profiles are provided in Figure S10 (Supporting Information). Well-defined voltage plateaus ascribed to Fe^{2+}/Fe^{3+} and Mn^{2+}/Mn^{3+} redox couple were observed at lower current rate for all the samples retaining 140 mAh g^{-1} at C/10. An increased ohmic polarization was evident at higher currents leading to a complete loss of capacity at 10 C in all the cells, however, the cycling trend in Figure 7(e) reveals the recovery of the initial capacity of about 140 mAh g^{-1} when lowering back the current at C/10, thus indicating satisfactory rate capability.[16] On the other hand, the cells containing the heavier cathodes showed lower capacity at high current rates starting from 1 C, thus suggesting lower stability caused by the stress of raising the currents, also ascribed to the possible deterioration of the electrodes.[29,62,64] The stability of the electrochemical Li^+ (de−)insertion process was further investigated by galvanostatic cycling at a constant current rate of C/2, after two activation cycles at C/10 with the corresponding voltage profiles reported in Figure S11 (Supporting Information). As expected from the mechanical bend test results, the lower loading electrode (*i.e.* 100 GSM) showed improved cyclability and capacity retention (i.e. 70% after 100 cycles, Figure 7(f)), while increased loading led to faster deterioration and capacity fade.[49] On the other hand, all the cells present coulombic efficiency of about 94% at the first activation cycle that increases and reaches 99% in the subsequent ones.

While 250 GSM is a substantial electrode loading, it is also worth considering that the low stability of the heavier electrode in half-cell configuration could be also affected by the presence of lithium metal which may favour possible side reaction and electrodes degradation that could instead be reduced in full cell configuration.[65] In this regard, the electrochemical performance of all the cells prepared with LMFP73-0.5%SWCNT samples with different loadings were tested in coin-type full cells by using graphite as anode material and a constant current of C/5 as referred to the cathode (1 C = 170 mA g_{cat}^{-1}). The negative to positive areal capacity ratio (N/P) was settled at 1.1 for all cells and the results are reported in Figure 8.

The gravimetric capacity upon cycling for the different mass loadings is reported in Figure 8(a) (corresponding voltage profiles are reported in Figure S12 Supporting Information), while the areal capacity is reported in Figure 8(b). The voltage profiles reflect the combination of the respective cathode and anode signatures, thus leading to a behaviour fully in line with the one related to LMFP73 half-cells, characterized by two voltage plateaus at about 3.4 and 4 V ascribed to Fe^{2+}/Fe^{3+} and

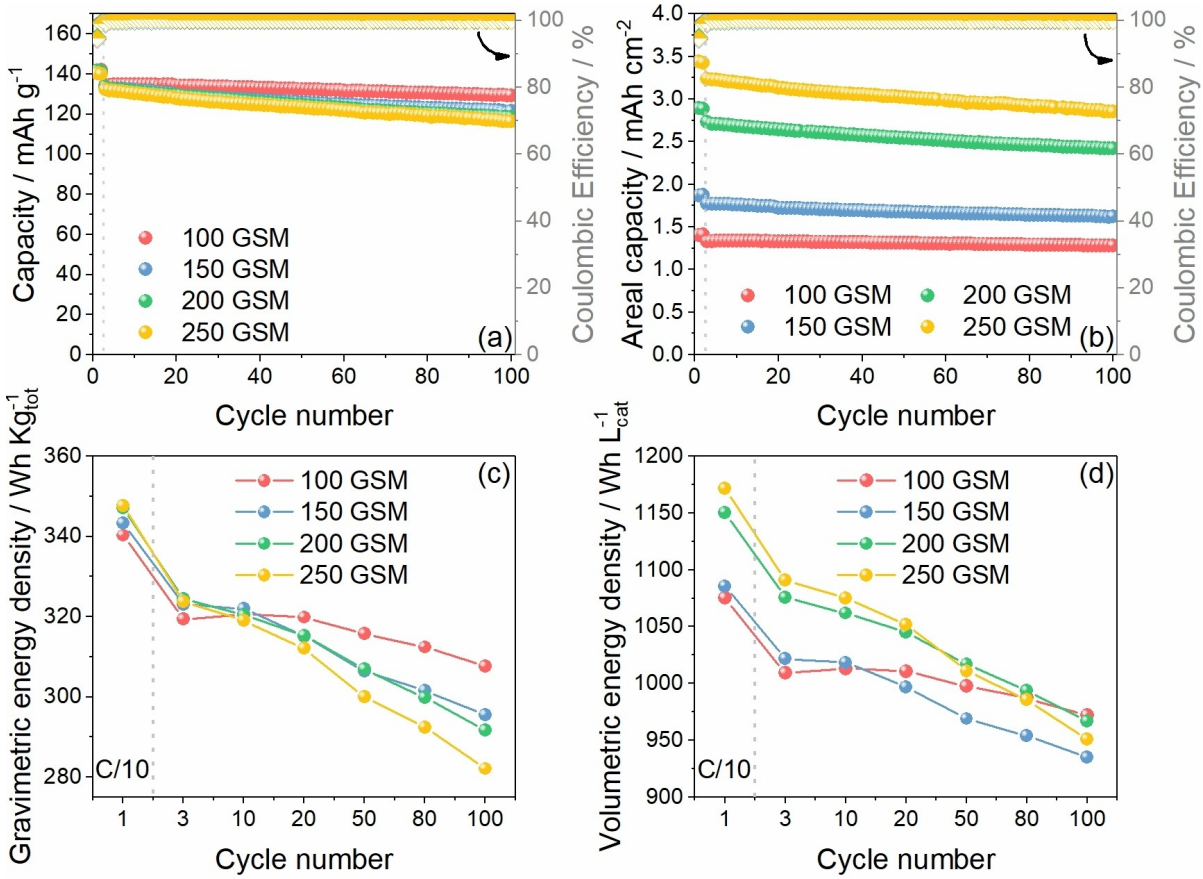

Figure 8. Electrochemical response of Graphite | LMFP-0.5%SWCNT coin cell-type full cells with different cathode loadings at 25 °C. Cycling trend of prolonged galvanostatic test performed at the constant current rate of C/5 (1 C = 170 mA g_{cat}^{-1}) after 2 activation cycles at C/10 with (**a**) gravimetric and (**b**) areal discharge capacity in left-hand side *y*-axes and coulombic efficiency in right-hand side *y*-axes. Voltage range 2.0–4.4 V. Trend of calculated (**c**) gravimetric and (**d**) volumetric energy density for different selected cycles.

Mn^{2+}/Mn^{3+} redox couples, respectively. Furthermore, the profiles reveal a maximum gravimetric capacity of about 135 mAh g^{-1} for all the samples, aligned with the rate capability data of the Li half-cells (see Figure 7(e)). The cycling trend of the full cells (Figure 8(a)) reveals similar stability for all the samples, confirming the improvement of the electrochemical response of heavier electrodes when avoiding the use of Li metal.[65] In particular, the cells exhibit remarkable coulombic efficiency of about 99.8% after activation cycles, with a maximum capacity retention of 96% for the cell adopting 100 GSM electrodes after 100 cycles. However, the cells containing electrodes with loadings of 200 and 250 GSM also show remarkable capacity retention of 89% and 86%, respectively. Furthermore, heavier electrodes exhibit higher areal capacity (Figure 8(b)) with values approaching 2.75 and 3.25 mAh cm^{-2} for the 200 and 250 GSM samples, respectively. Obtaining high areal capacities with satisfactory cycling stability is of outmost importance for the successful scaling up of cell prototype. Indeed, the industrially relevant loadings herein investigated also enable the matching with anodes presenting realistic loadings.[36,66]

Gravimetric (Figure 8(c)) and volumetric (Figure 8(d)) energy densities were calculated integrating the capacity as a function of the cell voltage for selected cycles dividing by the total mass of the coatings (anode + cathode, excluding the current collectors) and by the volume of the cathode composite layer, respectively. At the electrode level, the cells reveal high initial gravimetric energy density (of about 325 Wh Kg_{tot}^{-1}) for all the samples, which decreases as the cycles progress, due to the associated loss of capacity and different retention. Moreover, the volumetric energy density follows the same trend, with higher initial values of about 1090 Wh L_{cat}^{-1} for the cells adopting the higher areal loading. It is worth noting that the gravimetric energy density of the entire cell should be lower as the contribution of the other components (*e.g.* current collectors, electrolyte, and cell casing) on the total weight are not considered.[67] Nevertheless, the optimized electrode fabrication process developed has enabled satisfactory results also for high areal capacity electrodes, revealing the possibility to implement high loading cathodes in full cells with low losses in capacity and energy density when compared to lower loading cathodes. However, considering the lower structural stability of the 250 GSM cathodes, to mitigate potential detrimental issues upon cycling,[36] electrodes with 200 GSM loading were chosen as a suitable choice for the upscaling of the cell into SLP format.

Figure 9 reports the electrochemical response for SLP cells cycled at a constant current of C/2 referred to the cathode (1 C = 150 mA g_{cat}^{-1}), after 2 activation cycles at C/5. 0.1 Ah SLPs were obtained with an N/P ratio of 1.1 by using 0.6 g of electrolyte per cell. The cycling trend (Figure 9(a)) reveals remarkable cycling stability with a capacity retention of 93% after 100 cycles. Coulombic efficiency values of 97.1% are recorded after the first activation cycles, stabilizing to a value of 99.8% after 10 cycles.

The voltage profiles (Figure 9(b)) reveal the same features described above for full coin cells, with the presence of two well-defined voltage plateaus. Furthermore, the profiles exhibit a maximum capacity of about 110 mAh g^{-1} after activation, in full agreement with the rate capability data of the Li half-cells (see Figure 7(e)). However, considering the higher current rate adopted for the test (C/2 *vs* C/5), the gravimetric and volumetric energy densities (Figure 9(c)) of the cell are lower than the one reported for coin cells in Figure 8(c, d) (about 185 Wh Kg_{tot}^{-1} compared to 320 Wh Kg_{tot}^{-1}). Despite showing comparable trends, results suggest possible optimization of the SLP cell assembly steps, including improved electrode alignment and optimized electrolyte amount.[35,36,44] Indeed, it is worth noting that the electrochemical response is also cell format dependent.[66] SLPs for instance allow for degradation processes to occur in a more realistic cell environment. An example is represented by gas evolution, which may not affect substantially coin cell cycling, while may be more evident in upscaled cell formats. In addition, while this work focusses on the manufacturing-performance correlation, it is also important to consider that the electrolyte adopted has not been optimized and as such degradation mechanisms including potential manganese dissolution or instability of the SEI are still occurring in the developed cells. These processes are expected to be more relevant with increased loading and surface area of the anode exposed to the electrolyte. A comprehensive structure-property correlation study of the materials employed in battery research is of paramount importance, to then lead and guide performance optimization from a manufacturing point of view. A combination of these approaches is necessary to successfully translate research results from lab to industrial relevant scales, bridging the gap between academic and industrial research.[34,38]

3. Conclusions

In this study, we evaluated the impact of adding SWCNTs dispersion to LMFP73 electrode formulations and examined how various slurry and electrode processing parameters influence the overall cell performance in lab-scale and industrially relevant SLP cells. The results identified LMFP-0.5%SWCNT and LMFP73-1%SWCNT as the most promising formulations for enhancing the electronic conductivity of the olivine cathode, showing low electronic resistivity, suitable electrode morphology, with homogeneous components distribution and good structural stability. Given the economic advantage of minimizing inactive components in electrodes, the 0.5%SWCNT formulation was further studied to explore the effects of mixing protocol, coating speed, viscosity, and solid content on electrochemical performance. Mixing protocol #2, a coating speed of 6 mm s^{-1}, and 46% solid content led to improved results. Additionally, the influence of electrode loading on cyclability was assessed using optimized electrodes in both Li half and full cells. While lower-loading electrodes (100 GSM) demonstrated higher cycling stability, high-loading electrodes (250 GSM) showed an initial capacity of 130 mAh g^{-1} when cycled in Li half-cells at C/5, with reasonable rate capability up to 2 C, though with limited stability, likely due to Li metal/electrolyte interphase instability and structural electrode stability. Full cells

Research Article
doi.org/10.1002/batt.202400645
Chemistry Europe
European Chemical Societies Publishing

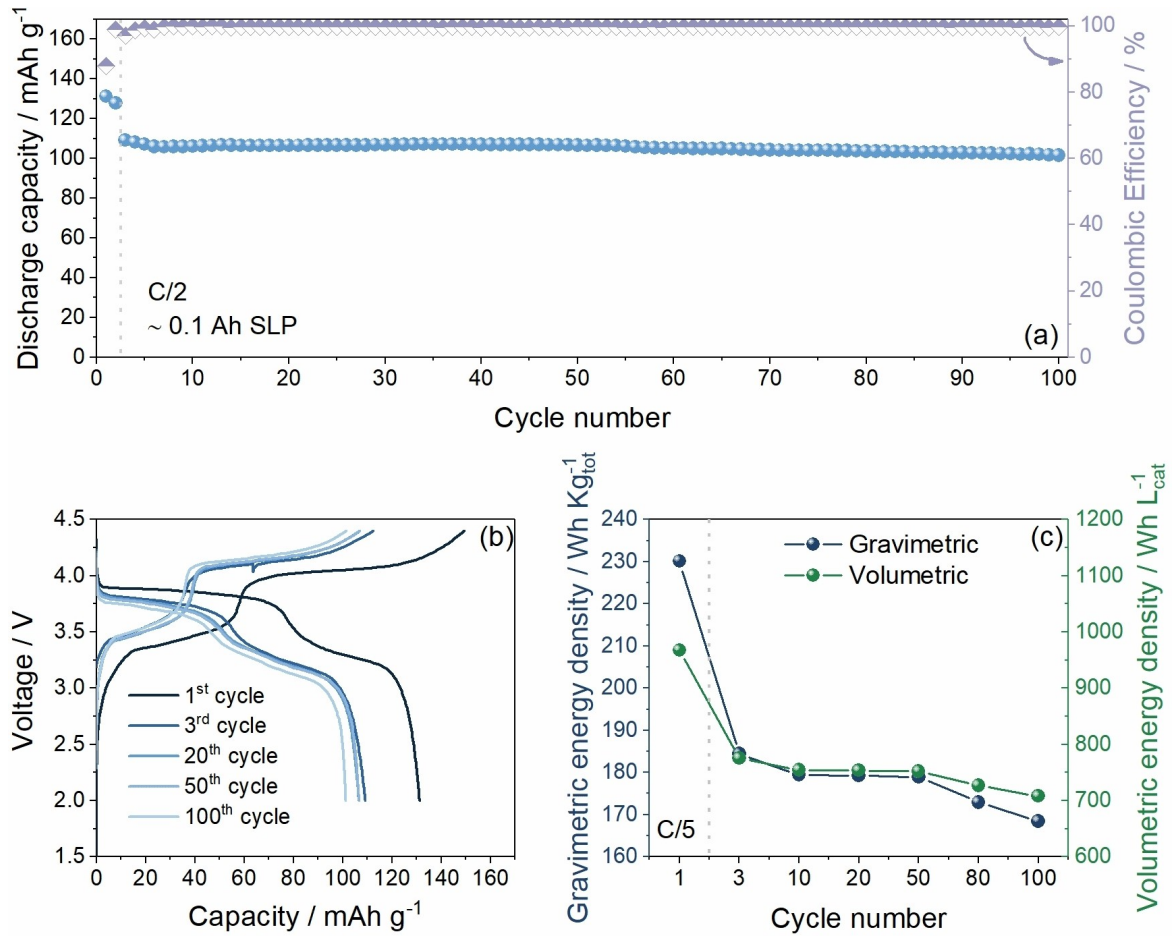

Figure 9. Electrochemical characterization of Graphite | LMFP-0.5 %SWCNT single layer pouch cell 25 °C. (**a**) Cycling trend and (**b**) selected voltage profiles of prolonged galvanostatic test performed at the constant current rate of C/2 (1 C = 150 mA g_{cat}^{-1}) after 2 activation cycles at C/5, with discharge capacity in left-hand side *y*-axes and coulombic efficiency in right-hand side *y*-axes. Voltage range 2.0–4.4 V. (**c**) Trend of calculated gravimetric and volumetric energy density for different selected cycles.

with graphite anodes showed greater stability compared to Li half-cells, with the 200 GSM sample offering the best balance in terms of mechanical properties, areal capacity (2.75 mAh cm^{-2}), and energy density (~320 Wh kg^{-1}). As a result, the 200 GSM cathode was chosen for 0.1 Ah SLP cell implementation, achieving a capacity of 110 mAh g^{-1} with 93 % retention after 100 cycles, though with lower energy density than in coin cells. These findings provide practical methods and processing parameters to bridge the gap between academic and industrial perspectives in electrode performance evaluation under realistic conditions. This work also underscores the critical role of the manufacturing-performance relationship on cell performance and cycling stability, particularly when scaling up from lab-scale to industrial cell formats, addressing challenges in improving performance with higher areal loadings, coating mechanical properties, practical electrode balancing, and electrolyte volume.

Experimental Section

LMFP73 powder characterization: The X-ray diffraction pattern of carbon-coated $LiMn_{0.7}Fe_{0.3}PO_4$ (LMFP73, Gelon, 1.5 wt.% of carbon) powder was collected using a Malvern PANalytical Aeris diffractometer (40 kV, 15 mA) with non-monochromated Cu Kα radiation (λ = 1.5408 Å). A Ni Cu Kβ filter, a Soller slit (0.04 rad), a divergence slit (1/4°), and a 13 mm X-ray mask were used on the incident beam side. An anti-scatter (9 mm) and Soller (0.04 rad) slits were used on the diffracted beam side. Scan was performed in Bragg-Brentano mode in the 2θ range from 10° to 75° at a rate of ~220 s $step^{-1}$ and a step size of 0.02°. Rietveld refinement of the pattern was carried out through the MAUD software[42] by using the reference parameters of $Li_{0.97}Mn_{0.77}Fe_{0.23}PO_4$ (*Pnma* space group, N. 62, ICSD #193643).[39] The weighted-profile (R_{wp}%) and goodness-of-fit (*GOF*) values were <4 and <2, respectively. Scanning electron microscopy (SEM) images were collected using a Tescan CLARA Ultra High Resolution (UHR-SEM) microscope with a Field Emission gun electron source. Energy dispersive X-ray spectroscopy (EDS) was carried out through the analyser of the former instrument (Oxford Instruments UltiMax 170). Analysis was carried out by applying an acceleration voltage of 5–10 kV.

Mixing and electrode fabrication: 50 g of LMFP73-*X*%SWCNT slurries with different solid contents were prepared by dispersing the active material, poly(vinylidene-fluoride) (PVdF 5130, Solef Solvay), carbon

black (C65 Imerys), and a SWCNTs dispersion (BATT TUBALL™; containing NMP >97%, PVdF 2%, dimethyl pyrrolidinone 0.05–0.39%, and SWCNTs TUBALL™ 0.4%) with a 95:2.5 : (2.5-*X*) : *X* (with $X=0$, 0.5, 1, 2.5) weight ratio, respectively, in N-methyl-pyrrolidone (NMP, Sigma Aldrich). SWCNTs present a length ≥ of 5 μm and a diameter of 1.6 (± 0.4) nm. The SWCNTs dispersion was used as received. See Table 1 in Results and Discussion section for formulation details. It is worth mentioning that the actual presence of SWCNTs per formulation ranges from 0.002% to 0.01% for the LMFP-0.5%SWCNT and LMFP2.5%SWCNT formulations, respectively, and that the PVdF content has not been adjusted in the slurry preparation with respect to the amount present in the SWCNTs dispersion. PVdF was pre-dissolved in NMP as an 8 wt% solution. The mixing was carried out by using an Intertronics (Kidlington, UK) Thinky mixer. The slurries were prepared following different mixing strategies described in the Results and Discussion section (see Figure 1 and Figure 4a). 50 g of Graphite V–H (BTR)[68–70] slurry with a 55% solid content was prepared by dispersing the active material, carboxymethyl cellulose (CMC, BVH8, Ashland), styrene-butadiene rubber (SBR, BM-451B, Zeon), and C65 with a 95.25:1.5:2.25:1 weight ratio, respectively, in deionised water. The CMC and the SBR were pre-dissolved in water as 2.5 wt% and 40 wt % solutions, respectively. The mixing was carried out with an Intertronics Thinky mixer. The viscosity of the slurries was measured using a TA Instruments HR20 rheometer equipped with a 40 mm roughened parallel plate and roughened lower plate, and a measuring gap of 500 μm, using a 25 °C constant temperature and a 0.001–5000 s^{-1} shear rate range.

LMFP73-*X*%SWCNT electrodes (with $X=0$, 0.5, 1, 2.5) were prepared by doctor blade casting on 15 μm aluminium foils (Avotec Steel) using an Erichsen draw down coater with a coating speed of 4 mm s^{-1}. The target electrode loading was 100 g m^{-2} (GSM). Subsequently, LMFP73-0.5%SWCNT electrodes, derived from both mixing strategies (50 g of total slurry), were casted at 2, 4, 6, and 8 mm s^{-1}, to optimize the coating speed, with a target electrode loading of ~50 GSM. Finally, optimized electrodes were prepared using 46% solid content, a coating speed of 6 mm s^{-1}, with target loadings of 100, 150, 200, and 250 GSM (100 g of total slurry). All the obtained coatings were dried at 80 °C on a hot plate and calendered at 85 °C (Innovative Machine Corp.) in order to achieve a target density ranged between 2.2 and 2.4 g cm^{-3} (equating to ~30–35% porosity). Graphite electrodes were prepared coating on 10 μm copper foils (Avotec Steel) with a coating speed of 6 mm s^{-1}, dried at 40 °C on a hot plate, and afterwards calendered to a target density of 1.5 g cm^{-3} (equating to ~30% porosity). The electrodes loading ranges from ~40 to ~105 GSM. Prior to cell assembly, electrodes were cut into disks (Ø 14.8 and 15 mm for LMFP73 and Graphite, respectively, for CR2032 coin cells and Ø 12 mm for Swagelok T-cells) and dried under dynamic vacuum using Glass Oven B-585 (BUCHI UK Ltd) at 120 °C for 12 hours.

Electrodes characterization and cell assembly: cx-SEM performed on the electrodes was collected with the above-described system. Before the measurements, homogeneous cross-sections were obtained using a HITACHI Ion Milling System (IM4000 plus) at an acceleration voltage of 4 kV for 90 minutes.

The resistivity of the electrode coatings was obtained by using an HIOKI RM2610 electrode resistance measurement system, with a 46-pin probe. Briefly, the system follows an inverse problem analysis and finite element modelling to measure composite volume resistivity (ρ_v) and interface resistance (R_{int}). By applying a constant current to the electrode sheet, the surface potential at various points can be measured. The system then models the electrode sheet and computes the potential on its surface considering composite volume resistivity (ρ_v) and interface resistance (R_{int}) as variables until the calculated potential matches with the observed potential. Once ρ_V and R_{int} are obtained, the final through-plane resistance (R_T) and following through-plane conductivity are calculated using Equation (1). Ten measurements for each sample are performed to assure the reliability of the data, with related confidence intervals and standard deviations of the means.

The mechanical properties of the coatings were studied through a cylindrical mandrel bend tester (BEVS 1603) using a 2-mm stainless-steel mandrel to observe possible cracks (see Table S2 for damage levels).[49] Two-electrode CR2032 coin cells were assembled using the prepared LMFP73 electrode as the working electrode and lithium metal foil (Ø 14.3 mm) or Graphite electrode as the counter electrode, with a H2325 Celgard® separator (Ø 16 mm). The Graphite|LMFP73 full cells were prepared by using a negative to positive (N/P) areal capacity ratio of 1.1 and 80 μL of electrolyte. Three-electrode Swagelok-type cells were assembled using LMFP73 as working electrode, lithium metal foil (Ø 12 mm) as counter and reference electrodes, and two glass fiber Whatman GF/A as separators (Ø 12.8 for the body and 12 mm for the upper part). A 1 M lithium hexafluorophosphate ($LiPF_6$) solution in a mixture of ethylene carbonate (EC): ethyl methyl carbonate (EMC) in a ratio of 3:7 (v/v%) with 1 wt% of vinylene carbonate (VC) as additive (Solvionic, France) was used as electrolyte for all electrochemical tests. All cells were assembled in an argon-filled glove box (MBraun) with a H_2O and O_2 content lower than 0.5 ppm.

Electrochemical characterization: CV measurements were carried out on Li|LMFP73-0%SWCNT coin type cells at a scan rate of 0.05 mV s^{-1} in the 2.8–4.4 V *vs.* Li^+/Li potential range. GITT experiments were performed using three-electrode Swagelok-type Li|LMFP73-0%SWCNT cell after four activation galvanostatic cycles carried out at 0.1 C current rate (1 C = 170 mA g^{-1}) in the potential range of 2.8–4.4 V *vs.* Li^+/Li. The titrations were performed by applying current pulses of 17 mA g^{-1} for 1430 s, followed by potential relaxation steps of 1 h at the open circuit. The operation conditions have been decided based on the activation cycles. Galvanostatic cycles were performed on Li|LMFP73-*X*%SWCNT ($X=$ 0%, 0.5%, 1%, 2.5%) and on Li|LMFP-0.5%SWCNT (loading 100, 150, 200, 250 GSM) coin type cells at the constant current rate of C/5 (1 C = 170 mA g^{-1}) and C/2 after 2 activation cycles at C/10, respectively. Rate capability tests were performed at increasing current rate by running 5 cycles at C/20, C/10, C/5, C/2, 1 C, 2 C, 5 C, 10 C, and finally lowering back the current to C/20 for Li|LMFP-*X*% SWCNT cells, while for Li|LMFP73-0.5%SWCNT cells the measurement was conducted in the same condition using C/10 as the starting and final current. Furthermore, alternate current rate capability tests were performed on LMFP73-*X*%SWCNT electrodes after 5 activation cycles at C/20 by charging the cell at C/10 and subsequently discharging it at C/5, C/2, 1 C, 2 C, 3 C, 4 C, 5 C, and 10 C. All galvanostatic measurements above described have been conducted in the 2.8–4.4 V voltage range. Galvanostatic cycles on the Graphite|LMFP73-0.5%SWCNT coin cell type full cells were performed at the constant current rate of C/5 (1 C = 170 mA g_{cat}^{-1}) after 2 activation cycles at C/10 in the 2.0–4.4 V voltage range. The reported results are obtained from the average of at least two measurements for each electrochemical test to confirm the reproducibility and reliability of the data. The GITT measurements were carried out by using a VMP-3 multichannel electrochemical workstation (Bio-Logic), while the CV and the cycling tests were performed by using a battery tester (BCS-805, Bio-Logic). All the electrochemical tests were carried out in a climatic chamber (Binder oven) at 25 °C.

Single layer Pouch (SLP) cells assembly and testing: SLP cells were assembled in a dry room, with a dew point lower than −40 °C, using a 33.2 cm^2 LMFP73-0.5%SWCNT electrode with a loading of 200 GSM as cathode and a 35 cm^2 Graphite electrode as anode, stacked between a H1609 Celgard® separator. Aluminium and

nickel-plated copper tabs of dimensions 0.2×8×60 mm (Cambridge Energy Solutions Ltd.) were used at the cathode and anode side, respectively. The stack was then sealed in aluminium laminate pouch bag material then vacuum filled with a slight excess of calculated amount of electrolyte of ~0.6 g (5 g Ah^{-1} consisting of the same solution above indicated). Cells were compressed between two Perspex plates with a layer of precision thickness polyurethane foam positioned on top and at the bottom of the cell to evenly distribute compression pressure across the electrode stack. Prior testing, cells were rested for 5 hours inside a Binder climatic chamber at 25 °C. Galvanostatic cycles were performed at a constant current rate of C/2 (1 C = 150 mA g_{cat}^{-1}) after 2 activation cycles at C/5 between 2.0–4.4 V voltage range and using an N/P ratio of 1.1. All cycling tests were performed using a Bio-Logic battery tester at 25 °C.

Acknowledgements

LM, MC and IH acknowledge funding from Innovate UK (Faraday Battery Challenge Round 5 Innovation: CR&D) – project number 10048444 (CONSTELLATION – CONstruction of Smart Three-dimensional ELectrode Lithium-ion bATteries via Industrial prOcesses and staNdards). AKH kindly acknowledges the funding from the WMG Centre High Value Manufacturing Catapult, University of Warwick, Coventry, United Kingdom.

Conflict of Interests

The authors declare no conflict of interest.

Data Availability Statement

The data that support the findings of this study are available from the corresponding author upon reasonable request.

Keywords: LMFP · Li-ion batteries · Formulation · Electrode manufacturing · Upscaling

[1] J. Neubauer, E. Wood, *J. Power Sources* **2014**, *259*, 262–275.
[2] P. S. Grant, D. Greenwood, K. Pardikar, R. Smith, T. Entwistle, L. A. Middlemiss, G. Murray, S. A. Cussen, M. J. Lain, M. J. Capener, M. Copley, C. D. Reynolds, S. D. Hare, M. J. H. Simmons, E. Kendrick, S. P. Zankowski, S. Wheeler, P. Zhu, P. R. Slater, Y. S. Zhang, A. R. T. Morrison, W. Dawson, J. Li, P. R. Shearing, D. J. L. Brett, G. Matthews, R. Ge, R. Drummond, E. C. Tredenick, C. Cheng, S. R. Duncan, A. M. Boyce, M. Faraji-Niri, J. Marco, L. A. Roman-Ramirez, C. Harper, P. Blackmore, T. Shelley, A. Mohsseni, D. J. Cumming, *Journal of Physics: Energy* **2022**, *4* (4), 042006.
[3] P. T. Moseley, J. Garche, *Electrochemical Energy Storage for Renewable Sources and Grid Balancing*, Elsevier **2015**, 270–306.
[4] B. Scrosati, J. Hassoun, Y. K. Sun, *Energy Environ. Sci.* **2011**, *4* (9), 3287–3295.
[5] A. K. Padhi, K. S. Nanjundaswamy, J. B. Goodenough, *J. Electrochem. Soc.* **1997**, *144* (4), 1188–1194.
[6] J. B. Goodenough, K.-S. Park, *J. Am. Chem. Soc.* **2013**, *135* (4), 1167–1176.
[7] Y. Wang, P. He, H. Zhou, *Energy Environ. Sci.* **2011**, *4* (3), 805–817.
[8] L. Minnetti, V. Marangon, P. Andreotti, A. Staffolani, F. Nobili, J. Hassoun, *Electrochim. Acta* **2023**, *452*, 142263.
[9] H. Gupta, S. K. Singh, N. Srivastava, D. Meghnani, R. K. Tiwari, R. Mishra, A. Patel, A. Tiwari, A. L. Saroj, R. K. Singh, *ACS Appl. Energ. Mater.* **2021**, *4* (12), 13878–13889.
[10] F. Croce, A. D'Epifanio, J. Hassoun, A. Deptula, T. Olczac, B. Scrosati, *Electrochem. Solid-State Lett.* **2002**, *5* (3), A47–A50.
[11] A. Moretti, G. Giuli, F. Nobili, A. Trapananti, G. Aquilanti, R. Tossici, R. Marassi, *J. Electrochem. Soc.* **2013**, *160* (6), A940–A949.
[12] D. Di Lecce, R. Brescia, A. Scarpellini, M. Prato, J. Hassoun, *ChemSusChem* **2016**, *9* (2), 223–230.
[13] L. Minnetti, V. Marangon, J. Hassoun, *Adv. Sustainable Syst.* **2022**, *6* (5), 2100464.
[14] B. Zhang, X. Wang, H. Li, X. Huang, *J. Power Sources* **2011**, *196* (16), 6992–6996.
[15] Z. X. Nie, C. Y. Ouyang, J. Z. Chen, Z. Y. Zhong, Y. L. Du, D. S. Liu, S. Q. Shi, M. S. Lei, *Solid State Commun.* **2010**, *150* (1–2), 40–44.
[16] L. Yang, W. Deng, W. Xu, Y. Tian, A. Wang, B. Wang, G. Zou, H. Hou, W. Deng, X. Ji, *J. Mater. Chem. A* **2021**, *9* (25), 14214–14232.
[17] Y.-K. Hou, G.-L. Pan, Y.-Y. Sun, X.-P. Gao, *ACS Appl. Mater. Interfaces* **2018**, *10* (19), 16500–16510.
[18] Z. Lei, J. Wang, J. Yang, Y. Nuli, Z. Ma, *ACS Appl. Mater. Interfaces* **2018**, *10* (50), 43552–43560.
[19] T. Ruan, B. Wang, F. Wang, R. Song, F. Jin, Y. Zhou, D. Wang, S. Dou, *Nanoscale* **2019**, *11* (9), 3933–3944.
[20] D. Kong, H. Chen, F. Wu, R. Zhang, J. Li, Y. Mai, Y. Wei, J. Wang, X. Dai, *Electrochim. Acta* **2024**, *506*, 145060.
[21] S. W. Oh, S. T. Myung, S. M. Oh, K. H. Oh, K. Amine, B. Scrosati, Y. K. Sun, *Adv. Mater.* **2010**, *22* (43), 4842–4845.
[22] Y. Liu, J. Manuel, X. Zhao, A. K. Haridas, G. S. Chauhan, J. K. Kim, K. K. Cho, H. J. Ahn, J. H. Ahn, *Sci. Adv. Mater.* **2017**, *9* (7), 1266–1271.
[23] A. Varzi, C. Täubert, M. Wohlfahrt-Mehrens, M. Kreis, W. Schütz, *J. Power Sources* **2011**, *196* (6), 3303–3309.
[24] V. Marangon, E. Barcaro, L. Minnetti, W. Brehm, F. Bonaccorso, V. Pellegrini, J. Hassoun, *Nano Res.* **2023**, *16* (6), 8433–8447.
[25] Y. Gao, L. Zhang, S. Feng, W. Shen, S. Guo, *J. Solid State Electrochem.* **2018**, *22* (1), 285–292.
[26] V. A. Nguyen, C. Kuss, *J. Electrochem. Soc.* **2020**, *167* (6), 065501.
[27] G. Apachitei, M. Hidalgo, D. Dogaru, M. Lain, R. Heymer, J. Marco, M. Copley, *Batteries* **2023**, *9* (4), 192.
[28] D. W. Kim, S. M. Hwang, J. B. Yoo, Y. Kim, *ChemElectroChem* **2020**, *7* (12), 2621–2628.
[29] J. Holloway, F. Maddar, M. Lain, M. Loveridge, M. Copley, E. Kendrick, D. Greenwood, *Batteries* **2020**, *6* (4), 57.
[30] A. Yamada, M. Hosoya, S. C. Chung, Y. Kudo, K. Hinokuma, K. Y. Liu, Y. Nishi, *J. Power Sources* **2003**, *119–121*, 232–238.
[31] C. D. Reynolds, P. R. Slater, S. D. Hare, M. J. H. Simmons, E. Kendrick, *Mater. Des.* **2021**, *209*, 109971.
[32] M. E. Spahr, *Carbon-Conductive Additives for Lithium-Ion Batteries, in Lithium-Ion Batteries*, Springer New York, New York, NY, **2009**, pp. 1–38.
[33] M. F. V. Hidalgo, G. Apachitei, D. Dogaru, M. Faraji-Niri, M. Lain, M. Copley, J. Marco, *J. Power Sources* **2023**, *573*, 233091.
[34] I. Hasa, S. Passerini, K. Edstrom, P. Stevens, A. Romanello, R. Scipioni, E. Sheridan, *Transportation Research Procedia* **2023**, *72*, 3625–3632.
[35] W. B. Hawley, J. Li, *J. Energy Storage* **2019**, *25*, 100862.
[36] M. J. Lain, J. Brandon, E. Kendrick, *Batteries* **2019**, *5* (4), 64.
[37] R. Gupta, S. Saha, M. Tomar, V. K. Sachdev, V. Gupta, *J. Mater. Sci. Mater. Electron.* **2017**, *28* (7), 5192–5199.
[38] J. T. Frith, M. J. Lacey, U. Ulissi, *Nat. Commun.* **2023**, *14* (1), 420.
[39] E. Lyle, R. Vaeli, A. Dutta, M. Metzger, *J. Electrochem. Soc.* **2022**, *169* (6), 060526.
[40] X. Y. Li, B. Zhang, Z. G. Zhang, L. H. He, H. Li, X. J. Huang, F. W. Wang, *Powder Diffr.* **2014**, *29* (3), 248–253.
[41] B. H. Toby, *Powder Diffr.* **2006**, *21* (1), 67–70.
[42] L. Lutterotti, *Nucl. Instrum. Methods Phys. Res. Sect. B* **2010**, *268* (3–4), 334–340.
[43] B. J. Landi, M. J. Ganter, C. D. Cress, R. A. DiLeo, R. P. Raffaelle, *Energy Environ. Sci.* **2009**, *2* (6), 638.
[44] J. Li, J. Fleetwood, W. B. Hawley, W. Kays, *Chem. Rev.* **2022**, *122* (1), 903–956.
[45] P. Saxena, P. Shukla, *Adv Compos Hybrid Mater* **2021**, *4* (1), 8–26.
[46] C. D. Reynolds, S. D. Hare, P. R. Slater, M. J. H. Simmons, E. Kendrick, *Energy Technol.* **2022**, *10* (10), 2200545.
[47] W. B. Hawley, J. Li, *J. Energy Storage* **2019**, *26*, 100994.
[48] C. Reynolds, M. Faraji Niri, M. F. Hidalgo, R. Heymer, L. Román, G. Alsofi, H. Khanom, B. Pye, J. Marco, E. Kendrick, *Batteries & Supercaps* **2024**, *7* (2), e202300396.
[49] L. S. de Vasconcelos, R. Xu, J. Li, K. Zhao, *Extreme Mech Lett.* **2016**, *9*, 495–502.

[50] M. Abdollahifar, H. Cavers, S. Scheffler, A. Diener, M. Lippke, A. Kwade, *Adv. Energy Mater.* **2023**, *13* (40), 2300973.
[51] A. van Bommel, R. Divigalpitiya, *J. Electrochem. Soc.* **2012**, *159* (11), A1791–A1795.
[52] C. Seidl, S. Thieme, M. Frey, K. Nikolowski, A. Michaelis, *Batteries* **2024**, *10* (3), 105.
[53] Y. Liu, H. Zhang, Z. Huang, Q. Wang, M. Guo, M. Zhao, D. Zhang, J. Wang, P. He, X. Liu, M. Terrones, Y. Wang, *J. Alloys Compd.* **2022**, *905*, 164205.
[54] Z. Du, J. Li, M. Wood, C. Mao, C. Daniel, D. L. Wood, *Electrochim. Acta* **2018**, *270*, 54–61.
[55] S. Hamed, F. Obrezkov, S. Huotari, M. Colalongo, S. Mousavihashemi, T. Kallio, *J. Power Sources* **2024**, *608*, 234549.
[56] P. Sae-Oui, U. Thepsuwan, P. Thaptong, C. Sirisinha, *Adv. Polym. Technol.* **2014**, *33* (4) 21422.
[57] R. Malik, F. Zhou, G. Ceder, *Phys. Rev. B* **2009**, *79* (21), 214201.
[58] G. Kobayashi, A. Yamada, S. Nishimura, R. ichi, R. Kanno, Y. Kobayashi, S. Seki, Y. Ohno, H. Miyashiro, *J. Power Sources* **2009**, *189* (1), 397–401.
[59] W. Weppner, R. A. Huggins, *J. Electrochem. Soc.* **1977**, *124* (10), 1569–1578.
[60] L. Minnetti, L. Sbrascini, A. Staffolani, V. Marangon, F. Nobili, J. Hassoun, *J. Energy Chem.* **2024**, *96*, 300–317.
[61] D. Di Lecce, J. Hassoun, *J. Phys. Chem. C* **2015**, *119* (36), 20855–20863.
[62] C. Heubner, S. Maletti, O. Lohrberg, T. Lein, T. Liebmann, A. Nickol, M. Schneider, A. Michaelis, *Batteries & Supercaps* **2021**, *4* (8), 1310–1322.
[63] P. G. Balakrishnan, R. Ramesh, T. Prem Kumar, *J. Power Sources* **2006**, *155* (2), 401–414.
[64] V. Augustyn, J. Come, M. A. Lowe, J. W. Kim, P.-L. Taberna, S. H. Tolbert, H. D. Abruña, P. Simon, B. Dunn, *Nat. Mater.* **2013**, *12* (6), 518–522.
[65] W. Xu, J. Wang, F. Ding, X. Chen, E. Nasybulin, Y. Zhang, J. G. Zhang, *Energy Environ. Sci.* **2014**, *7* (2), 513–537.
[66] G. Bridgewater, M. J. Capener, J. Brandon, M. J. Lain, M. Copley, E. Kendrick, *Batteries* **2021**, *7* (2), 38.
[67] C. X. Zu, H. Li, *Energy Environ. Sci.* **2011**, *4* (8), 2614–2624.
[68] G. Apachitei, R. Heymer, M. Lain, D. Dogaru, M. Hidalgo, J. Marco, M. Copley, *Batteries* **2023**, *9* (10), 518.
[69] A. S. Menon, N. Shah, J. A. Gott, E. Fiamegkou, M. J. W. Ogley, G. J. Páez Fajardo, N. Vaenas, I. Ellis, N. Ravichandran, P. Cloetens, D. Karpov, J. M. Warnett, P. Malliband, D. Walker, G. West, M. Loveridge, L. F. J. Piper, *Operando X-Ray and Postmortem Investigations. PRX Energy* **2024**, *3* (1), 013004.
[70] E. Guk, M. F. Niri, T. A. Vincent, G. Apachitei, C. Briggs, B. Gulsoy, S. Chao, Z. Guo, J. E. H. Sansom, J. Marco, *J. Power Sources* **2024**, *614*, 235063.

Manuscript received: September 30, 2024
Revised manuscript received: December 6, 2024
Accepted manuscript online: December 12, 2024
Version of record online: ■■, ■■

RESEARCH ARTICLE

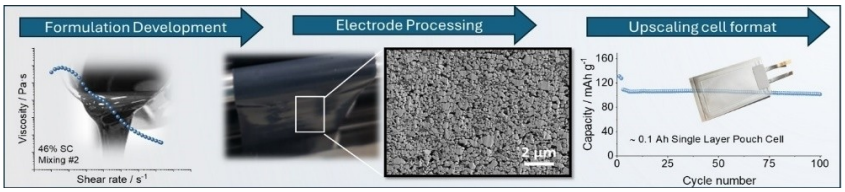

A manufacturing-performance correlation investigation: This study identifies optimal coating parameters for $LiMn_{0.7}Fe_{0.3}PO_4$ (LMFP) cathodes, offering practical methods to bridge the gap between academic research and industrial applications. Mixing strategy, slurry viscosity, solid content, coating speed, and electrode loading were systematically investigated to enhance the mechanical and microstructural properties of LMFP electrodes for application in single-layer pouch cells with graphite anodes.

*L. Minnetti, F. M. Maddar, A. K. Haridas, M. Capener, F. Nobili, I. Hasa**

1 – 18

Assessing Manufacturing-Performance Correlation On $LiMn_{0.7}Fe_{0.3}PO_4$ Electrodes For Application In Upscaled Li-Ion Battery Cells